

1 **Increased ecological resource variability during a critical transition**
2 **in hominin evolution**

3
4 One-sentence summary:

5 **Adaptations characteristic of early *Homo sapiens* prevailed during a shift to unstable**
6 **environment and less predictable resources.**

7
8 **AUTHORS:** Richard Potts^{1,2*}, René Dommain^{1,3}, Jessica W. Moerman¹, Anna K. Behrensmeyer⁴,
9 Alan L. Deino⁵, Simon Riedl³, Emily J. Beverly⁶, Erik T. Brown⁷, Daniel Deocampo⁸, Rahab
10 Kinyanjui², Rachel Lupien⁹, R. Bernhart Owen¹⁰, Nathan Rabideaux¹¹, James M. Russell¹², Mona
11 Stockhecke^{7,13}, Peter deMenocal⁹, J. Tyler Faith^{14,15}, Yannick Garcin¹⁶, Anders Noren¹⁷, Jennifer
12 J. Scott¹⁸, David Western¹⁹, Jordon Bright²⁰, Jennifer B. Clark¹, Andrew S. Cohen²¹, C. Brehnin
13 Keller²², John King²³, Naomi E. Levin²⁴, Kristina Brady Shannon¹⁷, Veronica Muiruri², Robin W.
14 Renaut²⁵, Stephen M. Rucina², Kevin Uno⁹

15
16 **AFFILIATIONS:**

17 ¹ Human Origins Program, National Museum of Natural History, Smithsonian Institution,
18 Washington, DC 20013, USA

19 ² Department of Earth Sciences, National Museums of Kenya, P.O. Box 40658, Nairobi 00100,
20 Kenya

21 ³ Institute of Geosciences, University of Potsdam, 14476 Potsdam, Germany

22 ⁴ Department of Paleobiology, National Museum of Natural History, Smithsonian Institution,
23 Washington, DC 20013, USA

24 ⁵ Berkeley Geochronology Center, Ridge Road, Berkeley, CA 94709, USA

25 ⁶ Earth and Atmospheric Sciences, University of Houston, TX 77204, USA

26 ⁷ Large Lakes Observatory and Dept. of Earth and Environmental Sciences, University of
27 Minnesota Duluth, Duluth, MN 55812, USA

28 ⁸ Department of Geosciences, Georgia State University, Atlanta, GA 30302, USA

29 ⁹ Lamont-Doherty Earth Observatory, Columbia University, Palisades, NY 10964, USA

30 ¹⁰ Department of Geography, Hong Kong Baptist University, Kowloon Tong, Hong Kong

31 ¹¹ Department of Chemistry, Rutgers University Newark, Newark, NJ 07109, USA

32 ¹² Dept. of Earth, Environmental, and Planetary Sciences, Brown University, Providence, RI,
33 02912, USA

34 ¹³ Department of Surface Waters-Research and Management, EAWAG, Überlandstr. 133, 8600
35 Dübendorf, Switzerland

36 ¹⁴ Natural History Museum of Utah, University of Utah, Salt Lake City, UT 84108, USA

37 ¹⁵ Department of Anthropology, University of Utah, Salt Lake City, UT 84112, USA

38 ¹⁶ Aix Marseille Univ, CNRS, IRD, INRAE, Coll France, CEREGE, 13545 Aix-en-Provence,
39 France

40 ¹⁷ Continental Scientific Drilling Coordination Office and LacCore Facility, Dept of Earth and
41 Environmental Sciences, University of Minnesota, Minneapolis, MN 55455, USA

42 ¹⁸ Department of Earth and Environmental Sciences, Mount Royal University, Calgary, Alberta
43 T3E 6K6, Canada

44 ¹⁹ African Conservation Centre, P.O. Box 15289, Nairobi 00509, Kenya

45 ²⁰ School of Earth and Sustainability, Northern Arizona University, Flagstaff, AZ 86011, USA

46 ²¹ Department of Geosciences, University of Arizona, Tucson, AZ 85721, USA

47 ²² Department of Earth Sciences, Dartmouth College, Hanover, NH 03755, USA

48 ²³ Graduate School of Oceanography, University of Rhode Island, Narragansett, RI 02882, USA

49 ²⁴ Department of Earth and Environmental Sciences, University of Michigan, Ann Arbor, MI
50 48109, USA

51 ²⁵ Department of Geological Sciences, University of Saskatchewan, Saskatoon, SK S7N 5E2,
52 Canada

53
54 *Corresponding author: pottsr@si.edu

55 **ABSTRACT:** Although climate change is widely considered to have been a large-scale driver of
56 African human evolution, landscape-scale shifts in ecological resources that may have shaped
57 novel hominin adaptations are rarely investigated. We use well-dated, high-resolution, drill-core
58 data sets to understand ecological dynamics associated with a major adaptive transition recorded
59 in nearby archeological sites. The core is ~24 km from outcrops that preserve evidence of the
60 replacement of Acheulean by Middle Stone Age (MSA) technological, cognitive, and social
61 innovations dated to between 500 and 300 thousand years ago (ka), contemporaneous with large-
62 scale taxonomic and adaptive turnover in mammal herbivores. Beginning ~400 ka, tectonic,
63 hydrological, and ecological changes combined to disrupt a relatively stable resource base,
64 prompting increasingly large and frequent fluctuations in freshwater availability, grassland
65 communities, and woody plant cover. Interaction of these factors offers a resource-oriented
66 hypothesis for the evolutionary success of MSA adaptations, which likely contributed to the
67 ecological flexibility typical of *Homo sapiens* foragers.

68
69 **MAIN TEXT**

70
71 **Introduction**

72
73 Hypotheses linking environmental change with human evolution have focused on temporal
74 correlations between global or regional climate change and major evolutionary benchmarks. For
75 African hominin evolution, one approach is to identify how increased aridity, humidity, or climate
76 variability induced by orbital forcing broadly coincided with, and thus potentially initiated, the
77 emergence of hominin adaptations and speciation events over time (1-5). It is not yet clear,
78 however, whether any of these general paleoclimate hypotheses account for critical transitions in

79 hominin evolution. A continuing challenge is to connect climate and environmental records with
80 water availability, food, and other ecological resources critical to energy acquisition, yet
81 susceptible to changes that may undermine an organism's existing adaptive strategies. Here we
82 integrate high-resolution drill core data with outcrop records from adjacent sub-basins in the
83 southern Kenyan Rift Valley to examine how shifts in landscape-scale ecological resources could
84 have influenced hominin adaptation during an interval of fundamental archeological and
85 paleontological change in this region.

86 The sedimentary record recovered by the Olorgesailie Drilling Project (core ODP-OLO12-
87 1A) from the Koora basin (1.8°S 36.4°E) provides evidence for changes in water availability,
88 vegetation, and overall resource landscapes associated with the demise of the Acheulean – the
89 longest enduring Paleolithic technology – and its replacement by early Middle Stone Age (MSA)
90 technology as documented in the adjacent Olorgesailie basin (1.5-1.6°S, 36.4-36.5°E; Fig. 1).
91 Olorgesailie preserves the oldest evidence currently known in East Africa of the permanent loss
92 of the Acheulean (defined by handaxes and other large cutting tools) and the emergence of MSA
93 behavioral innovations (6, 7). This transition involved new technologies, long-distance obsidian
94 transfer indicating resource exchange among interconnected social groups, and the use of coloring
95 material potentially related to enhanced symbolic capability (Table 1).

96 The onset of these behavioral innovations in the southern Kenya Rift occurred between
97 500 and 320 ka (Fig. 1) (8), an interval that overlaps the estimated time of genomic divergence
98 between *Homo sapiens* in Africa and the Neanderthal-Denisovan clade in Eurasia (9). The oldest,
99 widely acknowledged fossil evidence of *H. sapiens* (Jebel Irhoud, Morocco), dated roughly 320 to
100 300 ka (10), coincided temporally with the oldest East African MSA evidence at Olorgesailie.
101 Although other hominin species, such as *H. heidelbergensis* (or *H. rhodesiensis*, e.g., Kabwe,
102 Zambia; ref. 11) and *Homo naledi* (Rising Star Cave, South Africa; ref. 12) were also present in
103 Africa at this time, neither of these taxa is securely associated with MSA artifacts whereas the

104 MSA is widely associated from 300 ka onward with early *H. sapiens* (13, 14). Hominin remains
105 from southern Kenya dated 397 to 334 ka consist of poorly preserved teeth and a femoral shaft
106 from Lainyamok (Fig. 1A), which are metrically consistent with early *H. sapiens* but otherwise
107 cannot distinguish archaic and modern humans (15, 16). Other cranial remains of late middle
108 Pleistocene age in eastern Africa typically combine *H. sapiens* and archaic traits, yet such finds
109 are either poorly constrained chronologically (e.g., Eliye Springs KNM-ES 11693, Kenya,) or
110 <200 ka (e.g., Guomde Formation KNM-ER 3884, Kenya; Eyasi 1 and 2, Ngaloba LH 18,
111 Tanzania; Kibish Formation Omo 1 and 2, Herto BOU-VP-16/1, Ethiopia) (reviewed in ref. 17).

112 Our study does not presume that either the MSA or *H. sapiens* originated in the southern
113 Kenya rift. This region, however, has yielded what is currently the oldest record with precise
114 dating (8) where MSA behavioral innovations permanently replaced the Acheulean.

115 In the southern Kenya Rift the Acheulean-to-MSA archeological transition was
116 accompanied by a massive, ~85% turnover in mammalian species between ~394 ka and 320 ka
117 (7). As part of the turnover, previously dominant megaherbivores disappear from the record
118 (“megagrazers”: body mass >900 kg) while smaller, water-independent, mixed grazing/browsing
119 herbivores increased in abundance (Fig. 1D, table S1).

120 An important motivation of our study is that an erosional hiatus occurs in the Ologesailie
121 basin outcrop record between 500 and 320 ka – the interval in which the behavioral and faunal
122 transitions described above took place (Figs. 1, 2). A structurally controlled southward slope and
123 faulting episodes that created rift sub-basins have been recognized for some time in the southern
124 Kenya Rift (18). We thus reasoned that a drill core in the Koora basin adjacent to and directly
125 downstream from the Ologesailie basin could recover sediments preserving high-resolution
126 environmental data for the critical time window missing in the north. The present-day Koora
127 basin is an up to 6-km-wide, 40-km-long graben bounded by ~1-Ma horst blocks of 50 to 150 m
128 height above valley surface. The basin is filled with a sedimentary sequence that was drilled in its

129 northernmost location, closest to Olorgesailie basin outcrops. In fact, we note that the Olorgesailie
130 and Koora basins had demonstrable, though periodic, hydrological and paleoenvironmental
131 connections over time (Fig. 2), which facilitates relating the core environmental records to the
132 archeological and paleontological evidence from Olorgesailie.

133 An age model presented previously by our research team for the core (19) provides the
134 most precisely dated environmental record covering the past 1 Myr in East Africa. The 139-m-
135 long core spans the period from $\sim 1084 \pm 4$ ka to 83 ± 3 ka, based on the age model constrained by
136 ^{40}Ar - ^{39}Ar ages on 22 intercalated tephra layers and the Brunhes-Matuyama magnetic reversal (19,
137 20) (Fig. 1E, fig. S2; text S1). In this study we examine how spatially localized data from the core
138 can be connected to larger spatial scales of the regional environment and to the archeological and
139 faunal evidence from the adjacent Olorgesailie basin.

140 We emphasize that the core data concerning vegetation, lithology, and hydrology provide
141 evidence on a variety of spatial scales ranging from local to regional. The archeological data to
142 which we link the core records also reflect wider spatial scales beyond the excavations
143 themselves. Lithic sources used by the Olorgesailie hominins document an expansion of resource
144 acquisition substantially larger than the Olorgesailie basin itself (6). Obsidian used in MSA
145 technology was transported from multiple volcanic outcrop sources located in different directions
146 over distances of minimally 25 to 95 km from Olorgesailie, in contrast with ≤ 5 km distance of
147 stone transport typical of the Acheulean tool assemblages (6, 7; Table 1). Integrating these data
148 and observations with evidence of regional tectonism and landscape partitioning provides a
149 framework for connecting, at high geochronological resolution, the sequence of changing
150 resource landscapes with the critical transitions in hominin behavior and fauna.

151 Data compilations on human foraging behavior, which include more than 150 hunter-
152 gatherer societies from low-latitude environments, show that diet, foraging range, group mobility
153 and size, among other adaptive characteristics, are systematically related to environmental setting

154 (21-23). According to these ethnographic observations, hunter-gatherers tend to increase their
155 investment in technology, expand their range of resource acquisition, and rely on distant social
156 alliances and exchange networks in situations of heightened resource unpredictability and risk
157 (23, 24). Given that these responses in modern human foragers have parallels in the archeological
158 innovations of the Olorgesailie MSA (6, 7), we examined the core record to test the hypothesis
159 that decreased resource predictability could have been a factor in the early appearance of MSA
160 adaptations in the southern Kenya Rift. The specific question we address is whether MSA
161 behaviors replaced the Acheulean in this region during a period of increased resource fluctuation,
162 an ecological factor that could have more broadly shaped the emergence of observed adaptive
163 responses of *H. sapiens* foragers.

164
165

166 **Results**

167

168 The sediment core was recovered in the Koora basin at a location ~24 km south of the
169 Olorgesailie outcrops that preserve evidence of the large shifts in hominin behavior and faunal
170 communities discussed above. The core's trachytic basement rock is overlain by a complex
171 succession of diatomaceous, carbonate-rich, siliciclastic, and volcanoclastic fluvial and mostly
172 lacustrine sediments, with multiple intervals of pedogenic alteration (Fig. 2). Our analyses have
173 yielded environmental data spanning most of the past 1 Myr, including particularly high-
174 resolution data for the temporal window of interest between 500 and 300 ka. We focused on
175 exploring changes in the availability of ecological resources by reconstructing vegetation
176 dynamics, paleohydrology, and hydroclimatic signals.

177 **Ecological indicators**

178 The core datasets allow us to track the past availability of freshwater on the landscape, which is a
179 limiting factor for most mammal species in eastern Africa and therefore strongly affects
180 populations in the area (25). To examine past changes in water supply we employed a set of

181 paleohydrological proxies including sediment stratigraphy, diatom assemblage data (transfer
182 functions), XRF elemental profiles, and XRD mineralogy (Fig. 3A). Diatom-based records of
183 electrical conductivity (EC) and planktonic versus benthic taxa (diatom CA axis 1) were used to
184 reconstruct changes in Koora basin salinity and relative lake depth (26), respectively (Fig. 3A, fig.
185 S3), thus reflecting the availability of potable water contained in a lake source. We integrate these
186 paleohydrological records with evidence of 30 paleosols, each broadly estimated to represent
187 subaerial exposure of ~50 to ~5000 years duration on the basis of soil maturity and structure (19;
188 see Materials and Methods), which together indicate repeated lake-land transitions. Sedimentary
189 structures such as burrows that formed in subaerially exposed sediments document periods of
190 lowered water table down to several meters below the emergent land surface (table S2, text S2).
191 We measured the carbon isotopic composition of pedogenic carbonates ($\delta^{13}\text{C}_{\text{pc}}$) from the
192 paleosols and obtained values of between -1.28 and 2.03‰ (average 0.03‰), which consistently
193 indicate local C_4 grasslands during subaerial intervals (Fig. 3B). Based on the combined evidence,
194 we conclude that each emergent land surface represents a period of marked lake regression and
195 local to lake-basin-wide desiccation. Multiple lithological transitions between lacustrine
196 sediments and paleosols throughout the core can thus be explained by marked variations in water
197 supply to the Koora basin.

198 Vegetation is also a critical resource for many mammal species, especially herbivores, and
199 a primary determinant of habitat, dietary, and foraging opportunities. We reconstructed vegetation
200 cover and composition on local to regional scales by utilizing carbon isotopes of leaf waxes, bulk
201 organic matter, and pedogenic carbonates ($\delta^{13}\text{C}_{\text{wax}}$, $\delta^{13}\text{C}_{\text{org}}$, $\delta^{13}\text{C}_{\text{pc}}$) and also phytolith assemblage
202 data (Fig. 3B) (see Materials and Methods). The carbon isotope data are interpreted in terms of
203 the proportion C_3 to C_4 plants, with C_4 plants, mainly grasses, having higher water use efficiency
204 adapted to arid conditions (27).

205 These carbon isotope-based proxies were necessarily obtained from different lithologies;
206 they thus preserve vegetation signals representing different yet overlapping times periods and
207 varied spatial scales. Whereas the $\delta^{13}\text{C}$ signature of pedogenic carbonates reflects only a localized
208 signal preserved in dry and exposed land surfaces lacking sediment input (i.e., no aggradation),
209 these conditions resulted in poor preservation of leaf waxes and organic matter. Thus leaf wax
210 and bulk organic $\delta^{13}\text{C}$ samples were extracted from lacustrine sediments. The bulk organic $\delta^{13}\text{C}$
211 measurements contain a mixed signal of basin-scale terrestrial vegetation and aquatic biomass
212 (e.g., algae) originating from the lake itself. The source area of bulk organic $\delta^{13}\text{C}$ is smaller than
213 that of the leaf wax $\delta^{13}\text{C}$ samples because the transport of waxes is partly fluvial and partly
214 aeolian (wax aerosols), and the latter can result in long-distance dispersal. Leaf waxes are
215 primarily produced by terrestrial vascular plants; therefore, the sediment leaf wax $\delta^{13}\text{C}$ signal
216 reflects the past C_3/C_4 plant composition from the Koora basin and its catchment.

217 The phytolith data also record vegetation signals on local (during dry phases) to regional
218 (fluvial transport during wet phases) scales. An advantage of including phytolith morphotypes in
219 our analysis is that they can be resolved taxonomically (28, 29). From the phytolith assemblages
220 we determined the tree cover density index (D/P) and the phytolith index (Iph). The D/P ratio is
221 the proportion of woody dicotyledons (D) over grasses (Poaceae, P), which we use to estimate
222 woody plant cover on the paleolandscape (30, 31). The Iph index records the proportion of short
223 (Chloridoideae) and tall grasses (Panicoideae) in savanna ecosystems, with values of >20-40%
224 indicating short-grass dominance (29, 31). In Africa today, areas of higher water availability
225 generally favor woody vegetation and/or tall grasses (Panicoideae), whereas arid conditions favor
226 short grasses (Chloridoideae) (29), which allows us to link past vegetation composition with
227 paleohydrology.

230 **A shift in ecological resources**

231 The core record exhibits mostly subdued variability in both the lacustrine and terrestrial data sets
232 during its first ~500 kyr, followed by a 400-kyr-long interval of marked variability and ecological
233 disruptions (Fig. 3). The division of the record into two major variability phases is also illustrated
234 by a doubling of dry intervals of emergent land surface ($n = 9$ paleosols before 500 ka versus 20
235 paleosols after). Overall, the proxy data contain only weak orbital signals (11-17% of the
236 variance), dominated by the 100-ka eccentricity period in the lake depth reconstruction (diatom
237 CA axis 1), the XRF Si/K ratio, and D/P tree cover index (Fig. 4, fig. S4).

238 Between ~1 Ma and 470 ± 15 ka, intermediate to deep freshwater lakes prevailed in the
239 Koora basin as inferred from the diatom CA axis 1 and electrical conductivity reconstruction
240 (median EC $< 800 \mu\text{S}/\text{cm}$; Fig. 3A). These lake phases were interrupted by nine emergent land
241 phases represented by paleosols that lasted for ~1000 to ~5000 years (19). Most of these dry
242 phases occurred between 780 and 590 ka. However, the combined duration of all nine dry
243 episodes represents only ~5% of this 530-ka-long period based on the age model (19). The
244 evidence indicates that freshwater was generally available in the Koora basin (Fig. 3A) during the
245 period when Acheulean toolmakers were active at Olorgesailie.

246 A reliable freshwater supply would have sustained the predominantly water-dependent
247 fauna of the region up to ~470 ka (Fig. 1D). Prior to the major faunal and archeological
248 transitions (i.e., before 500 ka), intermediate values of the D/P tree cover index with a median of
249 1 (range 0.2-36; Fig. 3B; fig. S5) indicate a mix of woody and grassy vegetation typical for
250 African tall and short grass savannas (29). The stable isotope record for this interval shows
251 depleted $\delta^{13}\text{C}_{\text{Org}}$ values, ranging from -24.9 to -27.7‰ (average -26.4‰), which are typical for C_3 -
252 dominated vegetation consistent with the D/P values of mixed vegetation. Coupled with evidence
253 of intermediate-deep freshwater lakes, this vegetation composition points to relatively high
254 moisture levels during the first 500 kyr of the record. However, unexpectedly, we determine high

255 Iph values with a median of ~60%, indicative of the concurrent predominance of short grasses
256 (Chloridoideae; Fig. 3B), which typically prevail in arid grasslands and conditions of low soil
257 moisture (29). The concurrent predominance of short grasses suggests that vegetation was
258 influenced by factors beyond water availability (precipitation).

259 The prolonged freshwater period was disrupted at 470 ± 15 ka, initially by a ~5-kyr dry
260 episode followed by >60-kyr interval of shallow and saline lake conditions (median EC >5500
261 $\mu\text{S}/\text{cm}$; Fig. 3A), marking the transition to an interval of high environmental variability. During
262 the critical time window between 500 to 300 ka, eight intervals of desiccation are recorded as
263 paleosols, five of which are estimated to have lasted for ~5 kyr each (Fig. 3). The intervals
264 between these dry phases are approximately 68 kyr, 16 kyr, 19.5 kyr, 15 kyr, 5.5 kyr, 18 kyr, and
265 29 kyr long, which conform partly with precessional frequencies and partly with non-orbital
266 rhythms (fig. S4).

267 In concert with these more frequent wet-dry shifts, ecological resources began to fluctuate
268 more widely by ~400 ka in both terrestrial and aquatic environments. Each of the lake phases
269 during the critical window was distinct in terms of lake depth, salinity, diatom productivity and
270 composition (Si/K ratio; Fig. 3A, fig. S4). Together with the more frequent subaerial intervals,
271 these variable lake conditions point to large fluctuations in lake level and highly variable moisture
272 supply. Between $\sim 400 \pm 5$ ka and 320 ± 7 ka, the D/P tree cover index (0.1-10; median 0.7) reveals
273 rapid shifts between woody vegetation and grassland in line with varying water availability (Fig.
274 3B, fig. S5), consistent with assemblage-based ecological variability (fig. S6). This varying
275 woody plant cover is also evident in larger fluctuations of $\delta^{13}\text{C}_{\text{org}}$ (-27.4 to -22.3‰) and $\delta^{13}\text{C}_{\text{wax}}$ (-
276 34.5 to -22.9 ‰), suggesting shifts between C_3 - (100%) and C_4 - (~70%) dominated vegetation.
277 The grassland composition as inferred by the Iph index implies pronounced variation in tall- and
278 short-grass dominance and complete turnover between these two grassland types after 350 ± 8 ka
279 (Fig. 3B). From ~330 to ~250 ka the Koora basin was apparently dominated by open grassland

280 vegetation; few phytoliths of woody plants in this interval result in a low median D/P index of
281 0.15. These grasslands were either characterized by tall- or short-grass abundance but rarely of
282 mixed composition.

283 The Olorgesailie Acheulean-to-MSA transition and the major faunal turnover thus
284 coincided with the onset of an ecological landscape characterized by decreased reliability of
285 potable water and increased variability of grassland vegetation type beginning ~400 ka. The shift
286 from megagrazers to a predominance of smaller-bodied herbivores, with a higher proportion of
287 browsers and mixed feeders, suggests that change in the mammal community favored organisms
288 that could adjust to diverse and/or fluctuating vegetation and dietary resources (Fig. 1D). In
289 addition, the more water-independent mammal taxa present in the fauna by at least 320-300 ka in
290 the southern Kenya rift would have been more resilient to erratic freshwater availability.

291 Beginning ~250 ka, after these transitions occurred, the phytolith data indicate a shift
292 toward tall grass dominance (median I_{ph} <20%) and the return of woody plants but with highly
293 varying density. This vegetation change is also recorded by $\delta^{13}\text{C}_{\text{wax}}$, which exhibits its overall
294 largest fluctuations (between -32.9 and -18.4‰), thus suggesting complete turnover between C₃
295 and C₄ plant dominance (Fig. 3B, fig. S5). Frequent ecological disruptions continued based on the
296 recurrence of short dry intervals (n = 12, after 250 ka), strongly fluctuating lake depth, and more
297 frequent saline lake conditions (Fig. 3A).

298 **Discussion**

300 What factors could have led to the transitions in water and vegetation resources, the loss of
301 megagrazers, and the replacement of Acheulean by MSA behaviors? Although orbitally-paced
302 climate variability is well documented in many East African paleoclimate records (1-5), evidence
303 for orbital cyclicity in our core data is weak compared to the large, abrupt, and increasingly
304 frequent landscape changes we document. Our analyses show that rainfall variations during the
305 past 1 Myr were influenced by orbital pacing, mainly the eccentricity cycle, but temporal changes

306 in water availability and vegetation as recorded in the core cannot solely be explained by orbital
307 forcing. Millennial-scale climate variations have been demonstrated in Northern Hemisphere mid-
308 Pleistocene records (e.g., refs. 32, 33), but our indicator records at the current sampling resolution
309 have not yet revealed such variability or temporal correlation with events documented at higher
310 latitudes. The episodic prevalence of tall grasses (Fig. 3B: Iph), furthermore, is inconsistent with
311 progressive aridity, another prominent hypothesis often invoked to explain hominin evolutionary
312 change. By focusing on ecological resources rather than climate alone, our study suggests that a
313 combination of geological, climatic, and ecological factors directly influenced fundamental shifts
314 in hominin and faunal adaptations in the southern Kenya Rift.

315 Previous geological observations document extensive faulting throughout the region after
316 ~500 ka, manifested in the deep erosion of Olorgesailie Fm. outcrops to the north between ~499
317 ka and ~320 ka, and by drag-faulted sedimentary units that onlap horst walls post-499 ka at
318 Olorgesailie and post-397 ka at Lainyamok to the southwest (7, 16, 18, 34). Increased volcano-
319 tectonic activity is further indicated by an abrupt, nearly twofold rise in sedimentation rate and
320 increased volcanic tephra input in the Koora basin beginning ~400 ka (fig. S7) (19). One
321 consequence of this tectonism was increased topographic relief and basin compartmentalization
322 throughout the region (Fig. 1C, Fig. 2) (35). Tectonic development of the Koora basin's graben
323 morphology (Fig. 1B, C) over time would have resulted in amplified lake level fluctuations due to
324 higher sensitivity of graben-shaped lakes to changing moisture supply (36).

325 As a result, spatial heterogeneity in runoff, soil moisture, water availability, and
326 woody/grassy vegetation proportions was accentuated, with basins of varying size and
327 morphology potentially developing different sensitivities and divergent resource landscapes in
328 response to climate variations. Such interactions may account for contrasting environmental
329 histories apparent in the adjacent Magadi and Koora basins. The Magadi drill core provides the
330 only other relatively high-resolution environmental sequence in the region relevant to the past 1

331 Myr. Its vegetation record is interpreted as evidence of progressive aridification (37), whereas the
332 higher-resolution record presented here shows increased tall-grass dominance, mixed
333 woody/grassy vegetation, and fluctuations in C₃ vegetation in the interval from 500 ka to 300 ka
334 and after (fig. S8). This comparison indicates that, during the past 500,000 years, distinct
335 ecological zones and resource landscapes developed over a distance of less than 20 km between
336 the two rift basins (Fig. 1B). According to the relevant archeological data, distances of MSA
337 obsidian transport were minimally ~25 to 95 km as straight-line measures, which further suggests
338 that hominin foraging ranges and potential interactions among groups encompassed diverse
339 resource landscapes from the southern to the central Kenya Rift (6). This observation links the
340 hominin and faunal transitions in southern Kenya with spatial heterogeneity in ecological
341 resources in addition to the temporal variability shown here.

342 We note that the development of accentuated horst-graben topography also would have
343 dissected and diminished the spatial continuity of grazing landscapes. Persistent high grazing
344 pressure is known to transform broad areas of moist, wooded and tall grass habitats into extensive
345 short-grass grazing lawns (38-40). From ~1.0 Ma until the faunal turnover after 500 ka, the
346 megagrazers of the southern Kenya rift possessed craniodental specializations and estimated body
347 masses up to ~20% (e.g., the zebra *Equus oldowayensis*) to 400% (e.g., the baboon *Theropithecus*
348 *oswaldi*) larger than their modern counterparts (41, 42), which together suggests a unique grazing
349 community that had the capacity to establish and sustain short-grass grazing lawns despite the
350 prevailing moist conditions (39, 40).

351 We propose that the megagrazer decline and emergence of a different suite of mammal
352 species was a response to a more spatially fragmented and fluctuating resource base, which began
353 ~400 ka and thus within the critical window of faunal and archeological change (Fig. 5). A
354 combination of factors including accentuated topographic relief, climate variability, hydrological
355 subdivision of the region, and fragmentation of vegetation types could have created an interactive

356 cascade that diminished megagrazer populations in the region. This would have put specialized
357 grazers dependent on predictable short-grass and freshwater availability at a disadvantage relative
358 to mixed feeders and water-independent browsers, which increased between ~400 ka and 320 ka
359 (Fig. 1D) (8). Small obsidian points with retouched bases recovered from Olorgesailie
360 archeological sites are suggestive of projectile armaments dated ~320-307 ka (6), and thus
361 potentially indicate hominin predation as a possible influence on herbivore turnover in this region.
362 Since the definitive loss of megagrazer species in the region is recorded at 397-334 ka
363 (Lainyamok fauna: refs. 8, 43), the Olorgesailie MSA stone points could, however, reflect a
364 technological innovation for hunting smaller prey following the loss of megagrazer species (see
365 Fig. 1D).

366 We further suggest that compartmentalizing of the southern Kenya Rift into horst/graben-
367 delimited basins with quasi-independent resource dynamics also favored the transition to MSA
368 behavior. Even as mammalian populations experienced increased fragmentation of vegetation
369 types due to topographic partitioning of the landscape, evidence of widespread obsidian exchange
370 networks by ~320-295 ka (6, 8) imply that the MSA hominin groups actually became more
371 connected across the larger region. This response was potentially critical to their evolutionary
372 success in the changed resource regime. We hypothesize that MSA technological innovations and
373 distant resource exchange, sustained by symbolic communication, reflect an ability to respond to
374 increased instability in resource landscapes through risk mitigation, an adaptive strategy
375 ultimately characteristic of human foragers today (23, 24).

376 On the basis of our study, concurrent reshaping of hominin behavior and the faunal
377 community can be understood as distinctive responses to similar ecological stresses. We conclude
378 that although MSA adaptations may have originated elsewhere, they took hold in the southern
379 Kenya rift between 400 and 320 ka as a result of heterogeneity in selective conditions induced by
380 the marked shift to a temporally and spatially varied and less predictable resource landscape,

381 favoring hominin populations with resilient adaptations. Early evidence of this response suggests
382 that fundamental aspects of human adaptability had emerged by the time of our species' African
383 origin.

384 Our study prompts a wide range of questions for future investigation. We do not address
385 here the continent-wide demise of the Acheulean and its replacement by the MSA, but offer a
386 resource landscape hypothesis that could be tested in other parts of Africa. Last records of the
387 Acheulean occurred at various times in other African regions (e.g., 44), later than in the southern
388 Kenya Rift. The onset of the MSA, furthermore, is recorded at varying times in different places,
389 and MSA sites across the continent are associated with diverse environmental settings (14, 45). In
390 our study the oldest documented transition from Acheulean to MSA in eastern Africa occurred in
391 the context of repeated environmental disruptions. The hypothesis we present, which is limited to
392 a conjunction of factors in the southern Kenya Rift, should be examined elsewhere to see whether
393 the MSA flourished at the expense of the Acheulean under similar circumstances of ecological
394 disturbance. We recognize, however, that once MSA behaviors evolved, the adaptive flexibility
395 they conferred would have been advantageous and sustained in other locations where the MSA
396 spread, including in relatively stable habitats.

397 Integration of resource dynamics with regional tectonic and ecological history, as
398 exemplified by our study, also suggests a new direction in the search for causal processes that
399 shaped human evolution. Evolutionary adaptation entails not only the origin of behavioral
400 variations (7) but also their increase within a population and spread across a wider geographic
401 area. Studies of how environment may initiate evolution, therefore, need to further address the
402 processes that underlie adaptive change rather than assume, for example, that correlations
403 between evolution and either aridity, moisture, or variability provide a useful explanatory
404 hypothesis for any given change (5). Robust ecological theory as applied to human hunter-
405 gatherers and mammal herbivores provided the framework for investigating the potential

406 environmental influences on the hominin and faunal adaptations described here. We intend this
407 approach to be useful in motivating future research on how environmental dynamics may have led
408 to critical transitions in human evolution.

409

410 **Materials and Methods**

411

412 **Bayesian age model (C.B.K.)**

413 To constrain the absolute chronology of the ODP-OLO12-1A core, a high-resolution age-depth
414 model (fig. S2) was constructed using a Bayesian stochastic sampling approach to combine
415 quantitative age constraints from Ar-Ar geochronology, semi-quantitative minimum estimates for
416 the duration of observed exposure surfaces (depositional hiatuses), and the absolute constraint of
417 stratigraphic superposition. As described in (19), this Markov chain Monte Carlo model uses the
418 Metropolis algorithm to estimate the posterior age distribution for each centimeter of core depth.
419 At each step of the Markov chain, the previous age-depth model is perturbed by a symmetric
420 Gaussian proposal distribution, checked for stratigraphic superposition, and evaluated against the
421 combined quantitative constraints. Since adjacent proposals are highly correlated, this model was
422 run with a burn-in of 20,000,000 steps, and a sieved stationary distribution collected over the
423 subsequent 500,000,000 steps of the Markov chain.

424 **Age and proxy uncertainty analysis (S.Ri., Y.G.)**

425 Paleoenvironmental proxy data were translated into the time domain considering both proxy and
426 age model uncertainties by calculating uncertainty envelopes (shown in Fig. 3). Envelope width
427 along the time direction (x-axis) represents absolute age uncertainty based on the age model.
428 Envelope height in the proxy direction (y-axis) represents the analytical uncertainty of the proxy
429 data set. These uncertainty envelopes were generated by utilizing the full age model output: For
430 each proxy data point, its z-prime depth was assigned to the complete corresponding sieved age
431 distribution ($n = 25,000$) of the full age model at sample depth. (Fig. S2 shows the age model

432 uncertainties on the z-prime depth scale.) The analytical uncertainties of the proxy data were
433 assumed to have a normal distribution. These two individual uncertainties, in time domain (age
434 model) and proxy domain (analytical uncertainty), were used to generate 2d-histograms for each
435 data point. The obtained probabilities were then combined to composite probabilities per
436 continuous section of the data set. The environmental proxy records were treated as discontinuous
437 sections wherever the record was interrupted either by a paleosol occurrence (hiatuses), by
438 absence of core recovery (depth gaps), or by measurement gaps. A conservative discontinuity
439 criterion was further applied if neighboring data points were too remotely spaced, either in time
440 axis (threshold of 20 kyr) or in the depth axis (threshold of 10 m). For each obtained continuous
441 time interval, the obtained probability densities of individual data points were merged into a
442 composite probability. The resulting 68% and 95% confidence envelopes were ultimately
443 extracted from the obtained composite probability distributions. All the processing was
444 undertaken using MATLAB[®] (48).

445 **Spectral analysis (S.Ri.,P.deM.)**

446 To analyze orbital variability within the time series, Lomb-Scargle power spectra were calculated
447 because of their ability to work with unevenly-spaced data as represented in this drill core. The
448 absolute uncertainty of the age model was included by converting the proxy data into the time
449 domain for each individual z-prime–time distribution of the full age model ($n = 25,000$). Lomb-
450 Scargle power spectra were then calculated for each of the resulting time series of a specific
451 proxy (Fig. 4). Individual spectra ($n = 25,000$) were stacked to create one representative spectral
452 power density plot. This density plot shows the frequency spectrum of the proxy data, taking into
453 account time uncertainty in the full age model. Higher densities in the stacked spectrum denote
454 spectral powers which are consistent across the full age model.

455

456

457 **Diatoms (R.B.O.)**

458 Diatom samples were collected every 30 cm and where facies changed, with sampling intervals
459 reduced to 10 cm in relatively pure diatomites. Subsequent resampling of diatomaceous deposits
460 was carried out in order to reduce intervals for these sediments to 10–12 cm. Samples were
461 weighed and placed in a Calgon solution to assist dispersion. After washing with distilled water,
462 10% HCL was added to remove carbonates followed by further washing. Subsequently, 30%
463 H₂O₂ was added, followed by washing. In the last stage, a known number of microspheres (8 μm
464 diameter) were added to enable quantitative counting. Smear slides were prepared using *Naphrax*.
465 A minimum of 400 diatoms were counted, except where diatoms were rare in which case all
466 frustules were tallied. Diatoms were included in counts when more than half of a frustule was
467 present. Apices were counted for fragmentary long thin fragile taxa. Diatoms were identified at
468 1000× magnification with the supplementary aid of a Leo 1530 Field Emission Scanning Electron
469 Microscope. Identifications used standard taxonomic works, and especially Gasse (49, 50).
470 Correspondence Analyses (CA) were carried out using CANOCO 4.5 with taxa that formed ≥3%
471 in at least two samples, or ≥10% in at least one sample, included in analyses (n = 476). CA axis 1
472 tracks water depth, indicated by a high correlation with percentage of planktonic taxa, with
473 negative values associated with abundant *Aulacoseira* spp. and rare *Stephanodiscus* ($r = -0.959$, p
474 < 0.001) and positive values associated with benthic taxa (shallow). The percentage variance
475 explained by CA axis 1 is 68%. Environmental reconstructions were performed using ERNIE
476 software v. 1.2. Electrical conductivity for each sample (n = 476) was determined using the EDDI
477 “Combined Salinity Dataset”, and “Locally-weighted Weighted Averaging” (LWWA).

478 **Phytoliths and Pollen (R.K., R.D., S.M.R.)**

479 272 phytolith samples, 2-3cc in volume, were collected at 48-cm intervals with finer sampling at
480 ±10cm interval depending on core lithology. Samples were processed using a modified heavy
481 liquid floatation (51) as outlined in (52): (i) dissolution of carbonates with HCL; (ii) oxidation of

482 organic matter using HNO₃; (iii) heavy liquid floatation using Sodium Polytungstate at density of
483 2.4g/cm³; and (iv) gravitational removal of clay. The recovered fraction was mounted on
484 microscope slides using Entellan New medium. Freshly mounted slides were viewed under an
485 Olympus BX52 microscope at 400X magnification for 3D observation and counting. Because
486 most samples had low phytolith abundances, phytoliths >5 µm diameter in each sample were
487 counted and classified with aim of attaining a minimum of 200 grass short silica cells (GSSCs) to
488 acquire a statistically robust data set. Identification and classification of phytoliths largely
489 followed International code of phytoliths nomenclature (ICPN [53]) with refined GSSCs
490 classification based on (54-56), and with further consultation of other published studies (28, 52,
491 57-72). Phytolith data interpretation was based on two approaches: First, abundance diagrams
492 generated using TILIA program (73) showed variation in phytolith assemblages throughout the
493 core, which provided information about vegetation structure through time (52). Second, phytolith
494 indices were computed to determine changes in vegetation composition and climatic conditions.
495 Two phytolith indices were calculated: The D/P tree cover index is the ratio of woody
496 dicotyledons to all grasses and indicates changes in tree cover density through time (n = 218)
497 (30). The index (was computed by dividing rough globular phytoliths with the sum of Poaceae
498 phytoliths from the subfamilies Panicoideae, Chloridoideae, Arundinoideae and Aristidoideae
499 (dumbbell, cross, saddle, point-shaped and fan-shaped types). The Phytolith index (Iph) presents
500 the relative proportion of Chloridoideae (aridity affinity C₄ short grasses) versus Panicoideae
501 (moist affinity C₃₊₄ tall grasses), and was used to investigate temporal changes in this water
502 availability indicator (n = 183). The Iph index was computed as the ratio of Chloridoideae (saddle
503 morphotype) to the sum of Chloridoideae and Panicoideae (saddle, cross and dumbbell
504 morphotypes) (29). Cores were also sampled for pollen: Samples were processed at Ghent
505 University in Belgium following standard palynological procedure for concentrating pollen grains
506 (74). Slides mounted for pollen counts were examined at the National Museums of Kenya,

507 Department of Earth Sciences. Pollen was investigated using a Leitz microscope at x400. Pollen
508 preservation was very poor. Most slides had no pollen, but in rare cases one or two grains were
509 observed. Poor preservation might have been influenced by oxidation, high temperature, low
510 organic matter content, among other external factors.

511 **Identification of hiatuses and paleosols (E.J.B.)**

512 Thirty hiatuses marked by paleosols occur in core OLO12-1A and range from weakly to
513 moderately developed. These paleosols are identified by diagnostic soil features such as
514 bioturbation, soil peds, horizonation, and pedogenic carbonate. The top of each paleosol was
515 identified by a lithologic change and loss of ped structure, and the bottom of each paleosol by the
516 return of identifiable parent material lithology such as laminated lacustrine sediments. The
517 presence or absence and degree of development of these features allows for classification of the
518 paleosols using USDA Soil Taxonomy as paleo-Entisols, -Inceptisols, and -Vertisols (75). The
519 core ODP-OLO12-1A Entisols are very weakly developed soils with little or no evidence of soil
520 horizons, and they often contain relict bedding. The Inceptisols are more strongly developed than
521 Entisols with soil horizonation and ped formation, but lack distinguishing features that would
522 allow them to be classified as another soil order. The Vertisols are clay-rich soils with cracks,
523 pedogenic slickensides, and other vertic features that form as a result of shrinking and swelling of
524 clays during wetting and drying. These diagnostic features also allow for classification of these
525 paleosols into a paleosol maturity index modified from (76). This paleosol maturity index can
526 then be related to approximate the duration of pedogenesis as certain soil features form at
527 different time scales. For additional discussion of the paleosol characterization and estimates of
528 duration for the age modeling, see (19).

529 **$\delta^{13}\text{C}_{\text{wax}}$ and $\delta^{13}\text{C}_{\text{org}}$ (J.M.R., R.L., K.U., P.dM.)**

530 We measured the carbon isotopic composition of terrestrial leaf waxes ($n = 37$) following the
531 protocol outlined in (77). Lipids, which include leaf waxes, were extracted from freeze-dried and

532 homogenized bulk sediment using a DIONEX Accelerated Solvent Extractor 350 with
533 dichloromethane:methanol (9:1). The lipids were separated into neutral and acid fractions over an
534 aminopropylsilyl gel column using dichloromethane:isopropanol (2:1) and ether:acetic acid
535 (24:1). The acids were methylated using acidified methanol of known isotopic composition and
536 the resulting fatty acid methyl ethers (FAMES) were purified via silica gel column
537 chromatography. Relative abundances of the FAMES were quantified using an Agilent 6890 gas
538 chromatograph (GC) equipped with a HP1-MS column (30 m × 0.25 mm × 0.25 μm) and flame
539 ionization detector. Carbon isotopes were measured on an Agilent 6890 GC equipped with HP1-
540 MS column (30 m × 0.25 mm × 0.10 μm) coupled to a Thermo Delta V Plus isotope ratio mass
541 spectrometer (IRMS) with a reactor held at 1100°C at Brown University. The IRMS was run with
542 CO₂ of known isotopic composition as the external standard for normalization to Vienna PeeDee
543 Belemnite (VPDB), and a FAMES internal standard containing four homologues was measured
544 every 6th injection to monitor instrument performance and drift. Repeated measurement of the
545 internal standard yielded a standard deviation (1 sigma) of 0.20‰. Carbon isotope ratios were
546 measured in duplicate on each sample with a mean inter-sample difference of 0.20‰. All carbon
547 isotope measurements were corrected for the isotopic composition of the added methyl group,
548 where $\delta^{13}\text{C}_{\text{MeOH}} = -36.5\text{‰}$. We also analyzed the carbon isotopic composition of bulk sedimentary
549 organic matter ($\delta^{13}\text{C}_{\text{org}}$). The samples (n = 116) were acidified in 2 N hydrochloric acid (HCl) for
550 one hour at 80°C to remove carbonate minerals. The acid-treated samples were rinsed in
551 deionized water and centrifuged four times to remove excess HCl and were then lyophilized and
552 homogenized prior to isotopic analysis. The $\delta^{13}\text{C}_{\text{org}}$ values were measured using a Carlo Erba
553 Elemental Analyzer coupled to a Thermo Delta Plus isotope ratio mass spectrometer. The
554 analytical precision determined through replicate measurements of internal sediment standards
555 was 0.14‰. All $\delta^{13}\text{C}$ values are reported relative to the VPDB standard.

556 $\delta^{13}\text{C}_{\text{wax}}$ primarily records changes in the relative abundance of plants using the C_3
557 photosynthetic pathway (trees, shrubs, cool season grasses) versus plants using the C_4
558 photosynthetic pathway (warm season grasses and sedges) (78, 79). To quantify the relative
559 abundance of C_3 and C_4 vegetation, we used a two end-member mixing model that uses a $\delta^{13}\text{C}$ of
560 $n\text{-C}_{30}$ acids of -32.9‰ for the C_3 endmember and a $\delta^{13}\text{C}$ of $n\text{-C}_{30}$ acid of -19.0‰ for the C_4 end
561 member based on wax isotope measurements from the Turkana Basin in northern Kenya (80).
562 Measurements of the $\delta^{13}\text{C}$ of $n\text{-C}_{28}$ and $n\text{-C}_{30}$ acids from the Turkana Basin and various terrestrial
563 plants (81) indicate negligible offsets between these homologues allowing us to apply the
564 endmember $\delta^{13}\text{C}$ compositions from the $n\text{-C}_{30}$ acids. Our use of -32.9‰ for the C_3 endmember
565 assumes that closed canopy forests, which can produce waxes with much more depleted $\delta^{13}\text{C}$
566 values (82, 83), were not significant contributors to the waxes in the core. This assumption is
567 justified by the multiproxy data from our sediment core that indicate generally dry conditions
568 through the past 1 Ma. The bulk organic matter in lake sediment derives from both internal and
569 terrestrial sources, and its $\delta^{13}\text{C}$ records both aquatic carbon cycling as well as the $\delta^{13}\text{C}$ of
570 terrestrial organic inputs (84), largely driven by C_3/C_4 plant abundance. Although we cannot
571 determine the relative abundances of aquatic vs. terrestrial organic matter within the bulk
572 sedimentary organic matter in the ODP-OLO12-1A drill core, recent work has shown that the
573 $\delta^{13}\text{C}_{\text{org}}$ of tropical lakes responds strongly to changes in C_3/C_4 plant abundance (85, 86). We
574 interpret the $\delta^{13}\text{C}_{\text{org}}$ in the ODP core to reflect both aquatic ecosystem carbon cycling and C_3/C_4
575 plant abundance.

576 $\delta^{13}\text{C}_{\text{pc}}$ (J.W.M., N.E.L., E.J.B.)

577 Pedogenic carbonates (pc) ($n = 8$) were collected and analyzed for carbon isotopic composition
578 from the Bk horizons (zones of accumulation of carbonate) of eight paleosols focused on the
579 interval from 642 ka to 261 ka. Pedogenic carbonate was collected at least 50 cm below the top of
580 each paleosol (or a conservative estimate of the top) in order to ensure that $\delta^{13}\text{C}$ values of

581 pedogenic carbonates ($\delta^{13}\text{C}_{\text{pc}}$) reflect the isotopic composition of vegetation and not that of
582 atmospheric CO_2 (87). These carbonates, which were at various stages of development, were
583 sampled throughout the Bk horizons of moderately well-developed paleosols, with ped
584 development and horizonation caused by the dissolution of carbonate and reprecipitation at depth.
585 These Bk horizons showed increased Ca content at depth in scanning XRF unrelated to the parent
586 material. These carbonates were also identified as pedogenic in origin by their size (≤ 2 cm),
587 micritic texture, and the incorporation of soil matrix into the carbonate material as they grew over
588 time. Pedogenic carbonates less than 50 cm below the top of the paleosol, larger than 2 cm, or
589 with sparry textures were excluded from analysis to avoid any potential for diagenetic alteration.
590 Samples were powdered, homogenized, and dried at 40°C for 24 hours prior to analysis. Powders
591 were digested in 100% phosphoric acid at 70°C in single reaction vessels using a NuCarb device.
592 Carbon and oxygen isotope ratios of the resultant CO_2 were analyzed on a Nu Perspective gas
593 source isotope ratio mass spectrometer at the University of Michigan - Ann Arbor. Although not
594 highlighted in this paper, $\delta^{18}\text{O}$ values of these samples are also reported here for completeness. A
595 calcite working standard was measured every sixth sample and at the beginning and end of each
596 analytical run, yielding a standard deviation of 0.03‰ (1σ) for $\delta^{13}\text{C}$ and 0.11‰ (1σ) for $\delta^{18}\text{O}$,
597 where $\delta = [\text{R}_{\text{sample}}/\text{R}_{\text{standard}} - 1] * 1000$. Carbon and oxygen isotope ratios of all samples were
598 normalized via two-point linear calibration using international standards NBS-18 ($\delta^{13}\text{C} = -$
599 5.014‰ ; $\delta^{18}\text{O} = -23.2\text{‰}$) and NBS-19 ($\delta^{13}\text{C} = 1.95\text{‰}$; $\delta^{18}\text{O} = -2.20\text{‰}$). For each paleosol with
600 pedogenic carbonate, powders from 2 to 9 unique carbonate samples were analyzed. Pedogenic
601 carbonate samples include distinct nodules collected at discrete depths in the core as well as
602 aggregates of less indurated carbonate material collected over 3 to 25 cm intervals within a single
603 Bk horizon, as denoted in sample IDs. Each unique sample was analyzed in duplicate, yielding a
604 mean inter-sample difference in $\delta^{13}\text{C}_{\text{pc}}$ of 0.14‰ and $\delta^{18}\text{O}_{\text{pc}}$ of 0.17‰ . The mean $\delta^{13}\text{C}_{\text{pc}}$ values
605 and 1-sigma standard deviations of the analyses from these multiple nodules are plotted in Fig. 3.

606 All $\delta^{13}\text{C}_{\text{pc}}$ and $\delta^{18}\text{O}_{\text{pc}}$ values are reported in per mil (‰) relative to the Vienna Pee Dee Belemnite
607 (VPDB) standard. Age designations for mean pedogenic $\delta^{13}\text{C}_{\text{pc}}$ values are shown at the mid-point
608 of paleosol age durations.

609 **X-Radiography and XRF core scanning (M.S., E.T.B.)**

610 The ITRAX X-ray fluorescence core scanner of the Large Lake Observatory, Duluth, MN, was
611 used to measure bulk concentrations of major elements (e. g., Si, K, Ca) on split core surfaces (n
612 = 12,218) and to create X-radiographic images. X-radiographs were collected with 0.2mm
613 resolution (step size), with 60 kV, 50 mA and exposure time ranging from 200-1500 msec. XRF
614 data were collected at 1-cm resolution (step size) using the Mo X-ray tube with 30 kV, 20 mA, 60
615 sec exposure time. Three NIST Certified Reference Materials or Standard Reference Materials
616 (SRM) with properties similar to the sediment cores were used to calibrate the elemental raw
617 counts. The Si/K ratio reflects diatom productivity and preservation. High (low) Si/K may be
618 interpreted to reflect an oligotrophic, relatively fresh (eutrophic, alkaline) lake at the time of
619 deposition. The good correlation of Si/K to diatom counts (by R.B.O. and V.M.) indicates an
620 insignificant influence of biogenic silica from phytoliths or of quartz. The times series of %Ca
621 (dominated by calcium carbonate content) can reflect autochthonous carbonate precipitation
622 within a lake and/or carbonate nodules formed during post-depositional early diagenesis or
623 pedogenesis. In sections that were not significantly affected by pedogenesis, we propose two
624 scenarios to interpret %Ca variability: in periods when both Si/K and Ca% are high, carbonate
625 precipitation was likely triggered by photosynthesis in a eutrophic, relatively fresh lake. By
626 contrast, in intervals of low Si/K and high %Ca, carbonate precipitation was likely triggered by
627 oversaturation in a relatively saline, alkaline lake.

628 **XRD (N.R., D.D.)**

629 Samples for X-ray diffraction (XRD) analysis were collected at 48-cm intervals and at higher
630 resolution within sections of laminated lacustrine muds. A total of 402 samples were oven dried at

631 40°C for 48 hours, then ground to fine powder using ball and pestle impact grinders or mortar and
632 pestle. At Georgia State University, the bulk mineralogy of core material was analyzed by powder
633 X-ray diffraction (XRD) using a Panalytical X'pert Pro MPD using CuK α radiation, in the range
634 5-70°2 θ , operating at 45kV and 40mA with a total scan time of 30 minutes. Powder diffraction
635 patterns were analyzed using PANalytical High Score software suite with reference to PDF-2
636 database (88, 89).

637
638 **SUPPLEMENTARY MATERIALS**

639 materials and methods

640 fig. S1. Lithological key

641 fig. S2. Bayesian age model for core OLO12-1A on the z-prime depth scale

642 fig. S3. Electrical Conductivity (EC) (n = 476) of paleolake waters derived from a transfer
643 function approach based on diatom data

644 fig. S4. Earth's orbital cycles in comparison to key datasets from core ODP-OLO12-1A

645 fig. S5. Vegetation proxy results for core ODP-OLO12-1A

646 fig. S6. Interassemblage variability in (A) diatom taxa and (B) phytolith morphotypes, in samples
647 through the ODP core OLO12-1A, from ~1.084 Ma to ~83 ka

648 fig. S7. Derived sedimentation rate (in cm/yr) and percentage of volcanic glass based on complete
649 microscopic sediment composition

650 fig. S8. Divergent vegetation signals evident in (A) the Magadi basin pollen record (37) and (B)
651 the ODP-OLO12-1A Koora basin phytolith woody cover density record (D/P index, Fig.
652 3B) over the past 600,000 years

653 fig. S9. Expanded data sets indicating (A) water availability and (B) vegetation dynamics,
654 covering the critical window between 500 ka and 300 ka, from main text Fig. 3A and 3B.

655 table S1. Taxonomic composition of Acheulean- and MSA-associated mammalian faunas of the
656 Olorgesailie basin, categorized by body mass, water-dependence, and feeding strategy
657 based on functional morphology and modern taxonomic analogues

658 table S2. Minimum water table depth below exposure surfaces (last column) by stratigraphic
659 interval between 470.73 ka and 262.91 ka

660 text S1. Geochronology and core stratigraphy

661 text S2. Terrestrial trace fossils and minimum water table depth

662 text S3. Use of Si/K as an indicator of water availability

663 data table S3: Diatom taxa percentages on the drilled meters below surface depth scale

664 data table S4: Diatom CA axis 1 (dimensionless scores), on age model time scale with median
665 ages and uncertainties (a)

666 data table S5: Diatom electrical conductivity (EC), on age model time scale with median ages and
667 uncertainties (a)

668 data table S6: Phytolith counts and indices on age model scale with median ages and uncertainties
669 (a)

670 data table S7: Carbon and oxygen isotope values of pedogenic carbonates samples from Koora
671 basin core ODP-OLO12-1A, showing isotope data for each sample used to calculate the
672 mean paleosol $\delta^{13}\text{C}$ value, on meters below surface depth scale (see table S8)

673 data table S8: Mean pedogenic carbonate carbon and oxygen isotope data for paleosols in Fig. 3B
674 in Koora basin core ODP-OLO12-1A, on age model scale. Mean values are shown for
675 each paleosol in Fig. 3B.

676 data table S9: XRF core scanning for Si/K ratio on age model time scale with median ages and
677 uncertainties (a)

678 data table S10: XRD data on age model time scale with median ages and uncertainties (a)

679 data table S11: $\delta^{13}\text{C}$ -leafwax, percent C_3 leaf waxes on age model time scale with median ages
680 and uncertainties (a)

681 data table S12: $\delta^{13}\text{C}$ bulk organic matter on age model time scale with median ages and
682 uncertainties (a)

683 References (90-109)

684
685

686 **REFERENCES AND NOTES**

- 687 1. E. S. Vrba, in *Paleoclimate and Evolution, with Emphasis on Human Origins*, E. Vrba, G.
688 Denton, T. Partridge, L. Burckle, Eds. (Yale Univ. Press, New Haven, CT, 1995), pp. 24–45.
- 689 2. P. B. deMenocal, Plio-Pleistocene African climate. *Science* **270**, 53–59 (1995).
- 690 3. P. B. deMenocal, Climate and human evolution. *Science* **331**, 540-542 (2011).
- 691 4. M. H. Trauth, M. A. Maslin, A. L. Deino, M. R. Strecker, A. G. N. Bergner, M. Dühnforth,
692 High- and low-latitude forcing of Plio-Pleistocene East African climate and human evolution.
693 *J. Hum. Evol.* **53**, 475-486 (2007).
- 694 5. R. Potts, J. T. Faith, Alternating high and low climate variability: the context of natural
695 selection and speciation in Plio-Pleistocene hominin evolution. *J. Hum. Evol.* **87**, 5-20
696 (2015).
- 697 6. A.S. Brooks, J. E. Yellen, R. Potts, A. K. Behrensmeyer, A. L. Deino, D. E. Leslie, S. H.
698 Ambrose, J. R. Ferguson, F. d’Errico, A. M. Zipkin, S. Whittaker, J. Post, E. G. Veatch, K.
699 Foecke, J. B. Clark, Long-distance stone transport and pigment use in the earliest Middle
700 Stone Age, *Science* **360**, 90-94 (2018).
- 701 7. R. Potts, A. K. Behrensmeyer, J. T. Faith, C. A. Tryon, A. S. Brooks, J. E. Yellen, A. L.
702 Deino, R. Kinyanjui, J. B. Clark, C. M. Haradon, N. E. Levin, H. J. M. Meijer, E. G. Veatch,
703 R. B. Owen, R. W. Renaut, Environmental dynamics during the onset of the Middle Stone
704 Age in eastern Africa, *Science* **360**, 86-90 (2018).

- 705 8. A. L. Deino, A. K. Behrensmeyer, A. S. Brooks, J. E. Yellen, W. D. Sharp, R. Potts,
706 Chronology of the Acheulean to Middle Stone Age Transition in Eastern Africa, *Science* **360**,
707 95-98 (2018).
- 708 9. C. M. Schlebusch, H. Malmström, T. Günther, P. Sjödin, A. Coutinho, H. Edlund, A. R.
709 Munters, M. Vicente, M. Steyn, H. Soodyall, M. Lombard, M. Jakobsson, Southern African
710 ancient genomes estimate modern human divergence to 350,000 to 260,000 years ago.
711 *Science* **358**, 652-655 (2017).
- 712 10. D. Richter, R. Grün, R. Joannes-Boyau, T. E. Steele, F. Amani, M. Rué, P. Fernandes, J-P.
713 Raynal, D. Geraads, A. Ben-Ncer, J-J. Hublin, S. P. McPherron, The age of the hominin
714 fossils from Jebel Irhoud, Morocco, and the origins of the Middle Stone Age. *Nature* **546**,
715 293-296 (2017).
- 716 11. R. Grün, A. Pike, F. McDermott, S. Eggins, G. Mortimer, M. Aubert, L. Kinsley, R. Joannes-
717 Boyau, M. Rumsey, C. Denys, J. Brink, T. Clark, C. Stringer. Dating the skull from Broken
718 Hill, Zambia, and its position in human evolution. *Nature* **580**, 372–375 (2020).
- 719 12. P. H. Dirks, E. M. Roberts, H. Hilbert-Wolf, J. D. Kramers, J. Hawks, A. Dosseto, M. Duval,
720 M. Elliott, M. Evans, R. Grün, J. Hellstrom, A. I. Herries, R. Joannes-Boyau, T. V.
721 Makhubela, C. J. Placzek, J. Robbins, C. Spandler, J. Wiersma, J. Woodhead, L. R. Berger,
722 2017. The age of *Homo naledi* and associated sediments in the Rising Star Cave, South
723 Africa. *eLife* **6**: e24231.
- 724 13. S. McBrearty, A. S. Brooks, The revolution that wasn't: a new interpretation of the origin of
725 modern human behavior. *J. Hum. Evol.* **39**, 453-563 (2000).
- 726 14. J. Blinkhorn, M. Grove, The structure of the Middle Stone Age of eastern Africa. *Quat. Sci.*
727 *Rev.* **195**, 1-20 (2018).
- 728 15. P. Shipman, R. Potts, M. Pickford, Lainyamok: A new middle Pleistocene hominid site.
729 *Nature* **306**, 365-368 (1983).

- 730 16. R. Potts, P. Shipman, E. Ingall, Taphonomy, paleoecology and hominids of Lainyamok,
731 Kenya. *J. Hum. Evol.* **17**, 597-614 (1988).
- 732 17. C. Stringer, The origin and evolution of *Homo sapiens*. *Phil. Trans. R. Soc. B* **317**, 20150237
733 (2016).
- 734 18. B. H. Baker, J. G. Mitchell, L. A. J. Williams, Stratigraphy, geochronology and volcano-
735 tectonic evolution of the Kedong-Naivasha-Kinangop region, Gregory Rift Valley, Kenya. *J.*
736 *Geol. Soc.* **145**,107-116 (1988).
- 737 19. A. L. Deino, R. Dommain, C. B. Keller, R. Potts, A. K. Behrensmeyer, E. J. Beverly, J. King,
738 C. W. Heil, M. Stockhecke, E. T. Brown, J. Moerman, P. deMenocal, D. Deocampo, Y.
739 Garcin, N. E. Levin, R. Lupien, R. B. Owen, N. Rabideaux, J. M. Russell, J. Scott, S. Riedl,
740 K. Brady, J. Bright, J. B. Clark, A. Cohen, J. T. Faith, A. Noren, V. Muiruri, R. Renaut, S.
741 Rucina, K. Uno, Chronostratigraphic model of a high-resolution drill core record of the past
742 million years from the Koora Plain, south Kenya Rift: Overcoming the difficulties of variable
743 sedimentation rate and hiatuses. *Quat. Sci. Rev.* **215**, 213-231 (2019).
- 744 20. A. Cohen, C. Campisano, R. Arrowsmith, A. Asrat, A. K. Behrensmeyer, A. Deino, C.
745 Feibel, A. Hill, R. Johnson, J. Kingston, H. Lamb, T. Lowenstein, A. Noren, D. Olago, R. B.
746 Owen, R. Potts, K. Reed, R. Renaut, F. Schäbitz, J.-J. Tiercelin, M. H. Trauth, J. Wynn, S.
747 Ivory, K. Brady, R. O'Grady, J. Rodysill, J. Githiri, J. Russell, V. Foerster, R. Dommain, S.
748 Rucina, D. Deocampo, J. Russell, A. Billingsley, C. Beck, G. Dorenbeck, L. Dullo, D. Feary,
749 D. Garello, R. Gromig, T. Johnson, A. Junginger, M. Karanja, E. Kimburi, A. Mbuthia, T.
750 McCartney, E. McNulty, V. Muiruri, E. Nambiro, E. W. Negash, D. Njagi, J. N. Wilson, N.
751 Rabideaux, T. Raub, M. J. Sier, P. Smith, J. Urban, M. Warren, M. Yadeta, C. Yost, and B.
752 Zinaye, The Hominin Sites and Paleolakes Drilling Project: Inferring the environmental
753 context of human evolution from eastern African rift lake deposits. *Sci. Drill.* **21**, 1-16
754 (2016).

- 755 21. L.R. Binford, *Constructing Frames of Reference: An Analytical Method for Archaeological*
756 *Theory Building Using Ethnographic and Environmental Data Sets* (Univ. California Press,
757 Berkeley, 2001).
- 758 22. F. W. Marlowe, Hunter-gatherers and human evolution. *Evol. Anthropol.* **14**, 54-67 (2005).
- 759 23. R. L. Kelly, *The Foraging Spectrum: Diversity in Hunter-Gatherer Lifeways* (Cambridge
760 Univ. Press, New York, ed. 2, 2013).
- 761 24. R. Dyson-Hudson, E. A. Smith, Human territoriality: an ecological reassessment. *Am.*
762 *Anthropol.* **80**, 21-41 (1978).
- 763 25. D. Western, Water availability and its influence on the structure and dynamics of a savannah
764 large mammal community. *Afr. J. Ecol.* **13**, 265-286 (1975).
- 765 26. S. C. Fritz, S. Juggins, R. W. Battarbee, D. R. Engstrom, Reconstruction of past changes in
766 salinity and climate using a diatom-based transfer function. *Nature* **352**, 706-708 (1991).
- 767 27. E. A. Kellogg, C4 photosynthesis. *Curr. Bio.* **23**, R594-R599 (2013).
- 770 28. D. Barboni, R. Bonnefille, A. Alexandre, J.D. Meunier, Phytoliths as paleoenvironmental
771 indicators, West Side Awash Valley, Ethiopia. *Palaeogeogr. Palaeoclimatol. Palaeoecol.*
772 **152**, 87-100 (1999).
- 773 29. L. Bremond, A. Alexandre, O. Peyron, J. Guiot, Grass water stress estimated from phytoliths
774 in West Africa. *J. Biogeogr.* **32**, 311-327 (2005).
- 775 30. L. Bremond, A. Alexandre, C. Hély, J. Guiot, A phytolith index as a proxy of tree cover
776 density in tropical areas: Calibration with Leaf Area Index along a forest-savanna transect in
777 southeastern Cameroon, *Glob. Planet. Change* **45**, 277–293 (2005).
- 778 31. A. Alexandre, J.-D. Meunier, A.-M. Lézine, A. Vincens, D. Schwartz, Phytoliths: indicators
779 of grassland dynamics during the late Holocene in intertropical Africa. *Palaeogeogr.*
780 *Palaeoclimatol., Palaeoecol.* **136**, 213–219 (1997).

- 781 32. P. C. Tzedakis, V. Margari, D. A. Hodell, Coupled ocean–land millennial-scale changes 1.26
782 million years ago, recorded at Site U1385 off Portugal, *Glob. Planet. Change* **135**, 83-8
783 (2015).
- 784 33. M. Hyodo, B. Bradák, M. Okada, S. Katoh, I. Kitaba, D. L. Dettman, H. Hayashi, K.
785 Kumazawa, K. Hirose, O. Kazaoka, K. Shikoku & A. Kitamura, Millennial-scale northern
786 Hemisphere Atlantic-Pacific climate teleconnections in the earliest Middle Pleistocene. *Sci.*
787 *Rep.* **7**, 10036 (2017).
- 788 34. A. K. Behrensmeyer, R. Potts, A. Deino, The Oltulelei Formation of the southern Kenyan
789 Rift Valley: a chronicle of rapid landscape transformation over the last 500 kyr. *Geol. Soc.*
790 *Am. Bull.* **130**, 1474-1492 (2018).
- 791 35. B. H. Baker, in *Sedimentation in the African Rifts*, L. Frostick, R. Renaut, I. Reid, J.
792 Tiercelin, Eds. (Blackwell Scientific Publications, Oxford, 1986), pp. 45–57.
- 793 36. L. A. Olaka, E. O. Odada, M. H. Trauth, D. O. Olago, The sensitivity of East African rift
794 lakes to climate fluctuations. *J. Paleolimnol.* **44**, 629-644 (2010).
- 795 37. R. B. Owen, V. M. Muiruri, T. K. Lowenstein, R. W. Renaut, N. Rabideaux, S. Luo, A. L.
796 Deino, M. J. Sier, G. Dupont-Nivet, E. P. McNulty, K. Leet, A. Cohen, C. Campisano, D.
797 Deocampo, C-C. Shen, A. Billingsley, A. Mbuthia, Progressive aridification in East Africa
798 over the last half million years and implications for human evolution. *Proc. Natl. Acad. Sci.*
799 *U.S.A.* **115**, 11174-11179 (2018).
- 800 38. S. J. McNaughton, Ecology of a grazing ecosystem: the Serengeti. *Ecol. Monogr.* **55**, 259-
801 294 (1985).
- 802 39. C. Coetsee, W. D. Stock, J. M. Craine, Do grazers alter nitrogen dynamics on grazing lawns
803 in a South African savannah? *Afr. J. Ecol.* **49**, 62–69 (2011).

- 804 40. G. P. Hempson, S. Archibald, W. J. Bond, R. P. Ellis, C. C. Grant, F. J. Kruger, L. M.
805 Kruger, C. Moxley, N. Owen-Smith, M. J. S. Peel, I. P. J. Smit, K. J. Vickers, Ecology of
806 grazing lawns in Africa. *Biol. Rev.* **90**: 979–994 (2015).
- 807 41. L. Werdelin, W. J. Sanders, Eds., *Cenozoic Mammals of Africa* (Univ. California Press,
808 Berkeley, 2010).
- 809 42. R. Potts, Variability selection in hominid evolution. *Evol. Anthropol.* **7**: 81-96 (1998).
- 810 43. R. Potts, A. Deino, Mid-Pleistocene change in large mammal faunas of East Africa, *Quat.*
811 *Res.* **43**, 106-113 (1995).
- 812 44. J. D. Clark, Y. Beyene, G. WoldeGabriel, W. K. Hart, P. R. Renne, H. Gilbert, A. Defleur, G.
813 Suwa, S. Katoh, K. R. Ludwig, J.-R. Boisserie, B. Asfaw, T. D. White, Stratigraphic,
814 chronological and behavioural contexts of Pleistocene *Homo sapiens* from Middle Awash,
815 Ethiopia. *Nature* **423**, 747–752 (2003).
- 816 45. C. A. Tryon, J. T. Faith, Variability in the Middle Stone Age of eastern Africa. *Curr.*
817 *Anthropol.* **54**, S234-S254 (2013).
- 818 46. E. T. Brown, in: *Micro-XRF Studies of Sediment Cores: Applications of a Non-Destructive*
819 *Tool for the Environmental Sciences, Developments in Paleoenvironmental Research*, I.W.
820 Croudace, R.G. Rothwell, Eds. (Springer Netherlands, Dordrecht, 2015), pp. 267–277.
- 821 47. T. E. Cerling, J. G. Wynn, S. A. Andanje, M. I. Bird, D. K. Korir, N. E. Levin, W. Mace, A.
822 N. Macharia, J. Quade, C. H. Remien, Woody cover and hominin environments in the past
823 6 million years. *Nature* **476**, 51–56 (2011).
- 824 48. MathWorks. MATLAB® Release 2018a. (The MathWorks, Inc., 2018).
- 825 49. F. Gasse, *Les diatomées lacustres Plio-Pléistocènes du Gadeb (Ethiopie): systématique,*
826 *paléoécologie, biostratigraphie.* (Revue Algologique, Paris, 1980).
- 827 50. F. Gasse, *East African diatoms. Taxonomy, ecological distribution.* (J. Cramer, Stuttgart,
828 1986). *Bibliotheca Diatomologica*, vol. 11.

- 829 51. O. Katz, D. Cabanes, S. Weiner, A. M. Maeir, E. Boaretto, R. Shahack-Gross, Rapid
830 phytolith extraction for analysis of phytolith concentrations and assemblages during an
831 excavation: an application at Tell es-Safi/Gath, Israel. *J. Archaeol. Sci.* **37**, 1557–1563 (2010)
- 832 52. R. N. Kinyanjui, thesis, University of Witwatersrand (2018). <https://t.co/JxhDDR5olF>
- 833 53. M. Madella, A. Alexandre, T. Ball, International Code for Phytolith Nomenclature 1.0. *Ann.*
834 *Bot.* **96**, 253-260 (2005).
- 835 54. P. C. Twiss, E. Suess, R. M. Smith, Morphological classification of grass phytoliths. *Soil Sci.*
836 *Soc. Am. J.* **33**, 109-115 (1969).
- 837 55. P. C. Twiss, in *Phytolith Systematics, Emerging Issues*, G. Rapp, Jr., S. Mulholland, Eds.
838 (Plenum Press, New York, 1992), pp. 113-128.
- 839 56. L. Rossouw, thesis, University of the Free State (2009).
840 <https://scholar.ufs.ac.za/xmlui/handle/11660/4013>
- 841 57. G. Rapp, Jr., S. C. Mulholland, Eds., *Phytolith systematics: Emerging Issues* (Plenum Press,
842 New York, 1992).
- 843 58. G. G. Fredlund, L. T. Tieszen, Modern phytolith assemblages from the North American
844 Great Plains. *J. Biogeogr.* **21**, 321-335 (1994).
- 845 59. G. G. Fredlund, L. T. Tieszen, Calibrating grass phytolith assemblages in climatic terms:
846 application to Late Pleistocene assemblage from Kansas and Nebraska. *Palaeogeogr.*
847 *Palaeoclimatol. Palaeoecol.* **136**, 199-211 (1997).
- 848 60. D. Barboni, L. Bremond, R. Bonnefille, Comparative study of modern phytolith assemblages
849 from inter-tropical Africa. *Palaeogeogr. Palaeoclimatol. Palaeoecol.* **246**, 454-470 (2007).
- 850 61. F. Runge, The opal phytolith inventory of soils in central Africa—quantities, shapes,
851 classification, and spectra. *Rev. Palaeobot. Palynol.* **107**, 23–53 (1999).
- 852 62. D. R. Piperno, *Phytoliths: A Comprehensive guide for Archaeologists and Paleoecologists*
853 (AltaMira Press, Lanham, MD, 2006).

- 854 63. R. M. Albert, M. K. Bamford, D. Cabanes, Taphonomy of phytoliths and macroplants in
855 different soils from Olduvai Gorge (Tanzania) and the application to Plio-Pleistocene
856 palaeoanthropological samples. *Quat. Int.* **148**, 78–94 (2006).
- 857 64. D. Barboni, L. Bremond, Phytoliths of East African grasses: An assessment of their
858 environmental and taxonomic significance based on floristic data. *Rev. Palaeobot. Palynol.*
859 **158**, 29-41 (2009).
- 860 65. C. A. E. Strömberg, thesis, University of California Berkeley, 2003.
- 861 66. K. Neumann, A. Fahmy, L. Lespez, A. Ballouche, E. Huysecom, The Early Holocene
862 palaeoenvironment of Ounjougou (Mali): phytoliths in a multiproxy context. *Palaeogeogr.*
863 *Palaeoclimatol. Palaeoecol.* **276**, 87-106 (2009).
- 864 67. J. Mercader, T. Bennett, C. Esselmont, S. Simpson, D. Walde, Phytoliths in woody plants
865 from the Miombo woodlands of Mozambique. *Ann. Bot.* **104**, 91-113 (2009).
- 866 68. J. Mercader, F. Astudillo, M. Barkworth, T. Bennett, C. Esselmont, R. Kinyanjui, D. Laskin
867 Grossman, S. Simpson, D. Walde, Poaceae phytoliths from the Niassa Rift, Mozambique. *J.*
868 *Archaeol. Sci.* **37**, 1953-1967 (2010).
- 869 69. G. M. Ashley, D. Barboni, M. Dominguez-Rodrigo, H. T. Bunn, A. Z. P. Mabulla, F. Diez-
870 Martin, R. Barba, E. Baquedano, Spring and wooded habitats at FLK Zinj and their relevance
871 to origins of human behavior. *Quat. Res.* **74**, 304-314 (2010).
- 872 70. G. M. Ashley, D. Barboni, M. Dominguez-Rodrigo, H. T. Bunn, A. Z. P. Mabulla, F. Diez-
873 Martin, R. Barba, E. Baquedano, Paleoenvironmental and paleoecological reconstruction of a
874 fresh water oasis in savannah grassland at FLK North, Olduvai Gorge, Tanzania. *Quat. Res.*
875 **74**, 333-343 (2010).
- 876 71. R. N. Kinyanjui, thesis, University of Cape Town (2012).
877 http://www.pcu.uct.ac.za/sites/default/files/image_tool/images/192/Kinyanjui%202011.pdf

- 878 72. A. Novello, D. Barboni, L. Berti-Equille, J-C. Mazur, P. Poilecot, P. Vignaud, Phytolith
879 signal of aquatic plants and soils in Chad, Central Africa. *Rev. Palaeobot. Palynol.* **178**, 43-
880 58 (2012).
- 881 73. E. C. Grimm, *Tilia and Tiliagraph, vol. 101* (Illinois State Museum, Springfield, 1991).
- 882 74. K. Faegri, J. Iverson, *Textbook of Pollen Analysis* (Blackwell Scientific Publications, Oxford,
883 1975).
- 884 75. *Soil Survey Staff. Illustrated guide to soil taxonomy. v.1.* (USDA, NRCS, National Soil
885 Survey Center, Lincoln, Nebraska, 2014).
- 886 76. D. M. Cleveland, S. C. Atchley, L. C. Nordt, Continental sequence stratigraphy of the Upper
887 Triassic (Norian Rhaetian) Chinle strata, Northern New Mexico, U.S.A.: allocyclic and
888 autocyclic origins of paleosol-bearing alluvial successions. *J. Sediment. Res.* **77**, 909–924
889 (2007).
- 890 77. R. Lupien, J. M. Russell, C. Feibel, C. Beck, I. Castañeda, A. Deino, A. S. Cohen, A leaf wax
891 biomarker record of early Pleistocene hydroclimate from West Turkana, Kenya. *Quat. Sci.*
892 *Rev.* **186**, 225-235 (2018).
- 893 78. M. Bender, Variations in the $^{13}\text{C}/^{12}\text{C}$ ratios of plants in relation to the pathway of
894 photosynthetic carbon dioxide fixation. *Phytochemistry.* **10**, 1239-1244 (1971).
- 895 79. J.W. Collister, G. Rieley, B. Stern, G. Eglinton, B. Fry, Compound-specific $\delta^{13}\text{C}$ analyses of
896 leaf lipids from plants with differing photosynthetic pathway. *J. Organ. Geochem.* **21**, 619-
897 627 (1994).
- 898 80. K.T. Uno, P. J. Polissar, E. Kahle, C. Feibel, S. Harmand, H. Roche, P. B. deMenocal, A
899 Pleistocene palaeovegetation record from plant wax biomarkers from the Nachukui
900 Formation, West Turkana, Kenya. *Phil. Trans. R. Soc. B* **371**: 20150235 (2016).

- 901 81. Y. Chikaraishi, H. Naraoka, S. R. Poulson, Hydrogen and carbon isotopic fractionations of
902 lipid biosynthesis among terrestrial (C₃, C₄, and CAM) and aquatic plants. *Phytochemistry*
903 **65**, 1369-1381 (2004).
- 904 82. J. M. Russell, H. Vogel, B. L. Konecky, S. Bijaksana, Y. Huang, M. Melles, N. Wattrus, K.
905 Costa, J. W. King, Glacial forcing of central Indonesian hydroclimate since 60,000 yr B.P.
906 *Proc. Nat. Acad. Sci. USA* **111**, 5100-5105 (2014).
- 907 83. A. Vogts, H. Moossen, F. Rommerskirchen, J. Rullkötter, Distribution patterns and stable
908 carbon isotopic compositions of alkanes and alkane-1-ols from plant waxes of African rain
909 forest and savannah C₃ species. *Org. Geochem.* **40**, 1037-1054 (2009).
- 910 84. P. A. Meyers, J. L. Teranes, in *Tracking Environmental Change Using Lake Sediments*,
911 *Volume 2*, W. Last, J. Smol, Eds. (Kluwer, Dordrecht, 2001), pp. 239-270.
- 912 85. J. M. Russell, S. J. McCoy, D. Verschuren, I. Bessems, Y. Huang, Human impacts, climate
913 change, and aquatic ecosystem response during the past 2,000 years at Lake Wandakara,
914 Uganda. *Quat. Res.* **72**, 315-324 (2009).
- 915 86. M. Webb, P. A. Barker, P. M. Wynn, O. Heiri, M. van Hardenbroek, F. Pick, J. M. Russell,
916 A. W. Stott, M. J. Leng, Interpretation and application of carbon isotope ratios in freshwater
917 diatom silica. *J. Quat. Sci.* **31**, 300-309 (2016).
- 918 87. T. E. Cerling, Carbon dioxide in the atmosphere: evidence from Cenozoic and Mesozoic
919 paleosols. *Am. J. Sci.* **291**, 377-400 (1991).
- 920 88. D. M. Moore, R. C. Reynolds Jr., *X-ray Diffraction and the Identification and Analysis of*
921 *Clay Minerals*. (Oxford Univ. Press, New York, ed. 2, 1997).
- 922 89. G. W. Brindley, G. Brown, Eds., *Crystal Structures of Clay Minerals and their X-ray*
923 *Identification*, vol. 5 (Mineralogical Society of Great Britain and Ireland, London, 1980).
- 924 90. G. P. Hempson, S. Archibald, W. J. Bond, A continent-wide assessment of the form and
925 intensity of large mammal herbivory in Africa. *Science* **350**, 1056-1061 (2015).

- 926 91. G. Child, R. Parris, E. Le Riché, Use of mineralised water by Kalahari wildlife and its effects
927 on habitats. *Afr. J. Ecol.* **9**, 125-142 (1971).
- 928 92. W. F. de Boer, M. J. P. Vis, H. J. de Knegt, C. Rowles, E. M. Kohi, F. van Langevelde, M.
929 Peel, Y. Pretorius, A. K. Skidmore, R. Slotow, S. E. van Wieren, H. H. T. Prins, Spatial
930 distribution of lion kills determined by the water dependency of prey species. *J. Mammal.* **91**,
931 1280-1286 (2010).
- 932 93. R. Estes, *The Behavior Guide to African Mammals: Including Hoofed Mammals, Carnivores,*
933 *Primates* (Univ. California Press, Berkeley, 1991).
- 934 94. J. Kingdon, *The Kingdon Field Guide to African Mammals* (Academic Press, San Diego,
935 1997).
- 936 95. J. G. Ogg, in *The Geologic Time Scale 2012*, F. Gradstein, J. Ogg, M. Schmitz, G. Ogg, Eds.
937 (Elsevier, Boston, 2012), pp. 85–113.
- 938 96. J. L. Kirschvink, The least-squares line and plane and the analysis of palaeomagnetic data.
939 *Geophys. J. Int.* **62**, 699–718 (1980).
- 940 97. L. Sagnotti, Demagnetization Analysis in Excel (DAIE). *Ann. Geophys.* **56**, D0114 (2013).
- 941 98. J. D. A. Zijdeveld, in *Methods in Paleomagnetism*, D. Collinson, K. Creer, S. Runcorn, Eds.
942 (Elsevier, Amsterdam, 1967), pp. 254–286.
- 943 99. L. Tauxe, C. Badgley, Stratigraphy and remanence acquisition of a palaeomagnetic reversal
944 in alluvial Siwalik rocks of Pakistan. *Sedimentology* **35**, 697–715 (1988).
- 945 100. *A global overview of national regulations and standards for drinking-water quality* (World
946 Health Organization, Geneva, Switzerland, 2018).
- 947 101. P. Durringer, M. Schuster, J. F. Genise, H. T. Mackaye, P. Vignaud, M. Brunet, New termite
948 trace fossils: galleries, nests and fungus combs from the Chad basin of Africa (Upper
949 Miocene–Lower Pliocene). *Palaeogeogr. Palaeoclimatol. Palaeoecol.* **251**, 323–353
950 (2007).

- 951 102. J. F. Genise, *Ichnoentomology: Insect Traces in Soils and Paleosols*. Topics in Geobiology
952 37 (Springer, Switzerland, 2017).
- 953 103. E. M. Roberts, C. N. Todd, D. K. Aanen, T. Nobre, H. L. Hilbert-Wolf, P. M. O'Connor, L.
954 Tapanila, C. Mtelela, N. J. Stevens, Oligocene termite nests with *in situ* fungus gardens
955 from the Rukwa Rift Basin, Tanzania, support a Paleogene African origin for insect
956 agriculture. *PLoS ONE* 11(6): e0156847 (2016).
- 957 104. W. A. Sands, in *Laetoli: A Pliocene Site in Northern Tanzania*, M. Leakey, J. Harris, Eds.
958 (Oxford, New York. 1987), pp. 409–433.
- 959 105. J. J. Scott, R. W. Renaut, L. A. Buatois, R. B. Owen, Biogenic structures in exhumed
960 surfaces around saline lakes: an example from Lake Bogoria, Kenya Rift Valley.
961 *Palaeogeogr. Palaeoclimatol. Palaeoecol.* **272**, 176–198 (2009).
- 962 106. W. R. Tschinkel, The foraging tunnel system of the Namibian Desert termite,
963 *Baucaliotermes hainesi*. *J. Insect Sci.* **10**, 1-17 (2010).
- 964 107. S. C. Fritz, B. F. Cumming, F. Gasse, K. R. Laird, in *The Diatoms: Applications for the*
965 *Environmental and Earth Sciences*, J. Smol, E. Stoermer, Eds. (Cambridge University
966 Press, Cambridge, ed. 2, 2010), pp 186–208.
- 967 108. E. T. Brown, in *Micro-XRF Studies of Sediment Cores*, I. Croudace, Ed. (Springer,
968 Dordrecht, 2015), pp. 267-277.
- 969 109. J. Laskar, P. Robutel, F. Joutel, M. Gastineau, A.C.M. Correia, B. Levrard, A long-term
970 numerical solution for the insolation quantities of the Earth. *Astron. Astrophys.* **428**, 261–
971 285 (2004).

972
973
974 **ACKNOWLEDGMENTS**

975 The Olorgesailie Drilling Project gratefully acknowledges the National Museums of Kenya, the
976 Oldonyo Nyokie Group Ranch, and the Olorgesailie field team led by J.M. Nume and J.N.

977 Mativo. Research and drilling permits were provided by the Kenyan National Council for Science

978 and Technology, the Kenya Ministry of Petroleum and Mining, and the National Environmental
979 Management Authority of Kenya, and facilitated by the National Museums of Kenya. We thank
980 DOSECC Exploration Services for drilling supervision, Drilling and Prospecting International
981 (DPI) for drilling services, and the LacCore and CSDCO facilities (University of Minnesota) for
982 core handling, processing, and storage. Elevation data in Fig. 1 are based on the TanDEM-X
983 Science DEM (© DLR 2017) granted to S.Ri. by the German Space Agency. We are grateful for
984 discussions with colleagues of the Hominin Sites and Paleolakes Drilling Project (HSPDP), and
985 for comments by C. Stringer and anonymous reviewers.

986 **Funding:** Peter Buck Fund for Human Origins Research (Smithsonian), William H. Donner
987 Foundation (R.P.), the Ruth and Vernon Taylor Foundation (R.P.), Whitney and Betty MacMillan
988 (R.P.), National Science Foundation grants EAR 1322017 (A.L.D.) and EAR 1349599 (D.D.),
989 Swiss National Science Foundation grant P300P2 158501 (M.S.), Hong Kong Research Grants
990 Council (R.B.O., V.M), and the Smithsonian Human Origins Program (R.P).

991 **Author contributions:** R.P. and R.D. wrote the manuscript, with support from J.W.M., S.Ri.,
992 and A.K.B., and all authors provided edits and discussion. D.D., R.K., J.W.M., R.B.O., J.M.R.,
993 N.R., and M.S. contributed data for Fig. 3, and all authors contributed methods, analyses, and
994 discussion of data interpretations. R.D., S.Ri., Y.G., J.W.M., J.B.C., A.K.B., P. deM., J.T.F., and
995 R.P. developed the figures. R.P. directed and conceived the study. R.P. and A.K.B. selected the
996 drilling location. K.B.S., R.D., A.N., and J.B.C. provided field and laboratory support.

997 **Competing interests:** The authors declare no competing interests.

998 **Data and materials availability:** The data sets generated and analyzed during the current study
999 are available from the corresponding author on reasonable request. Source Data for Fig. 3 are
1000 provided in Supplementary data tables S3 through S12.

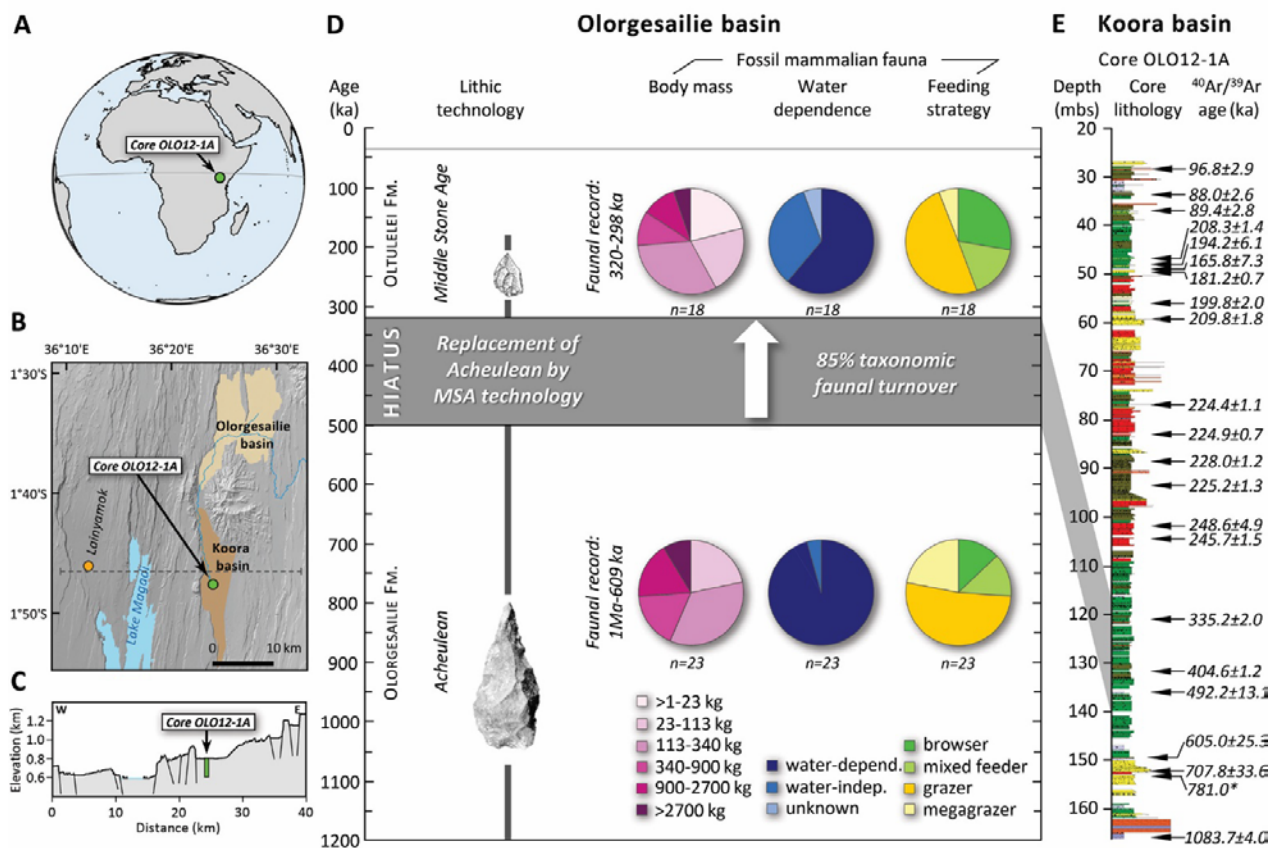
1001 **Table**

1002 **Table 1. Comparison of Acheulean technology (typified by handaxes and other large**
 1003 **cutting tools, or LCTs) and Middle Stone Age technology.** Behavioral and environmental
 1004 comparison includes: lithic source access and rock transport, pigment use, and environment
 1005 evidence based on observations in the Olorgesailie basin (6-8, 34), located 22-24 km from the
 1006 OLO12-1A drilling site. Predicted insolation dynamics (high or low climate variability) based
 1007 on (5).
 1008

<u>Comparisons</u> (Olorgesailie basin)	<u>Acheulean</u> Olorgesailie Fm (1.2 Ma to 499 ka)	<u>Middle Stone Age</u> lower Oltulelei Fm (~320 to 295 ka)
Artifact/tool size	Large tools, LCTs dominant	Smaller, diversified tools
Focus of lithic source access	Local volcanic rocks, coarse & fine-grain (98%)	Fine-grain rocks (e.g., obsidian, chert & fine-grain local volcanics)
Stone transport distances	No more than 5 km	Obsidian transfer: 25 - 95 km, from multiple directions
Altered & used pigments	No	Yes
Depositional regime (horst-graben formation)	Stable, aggrading system (lake/fluvial/floodplain)	Highly dynamic landscape (sub-basin cutting-and-filling)
East Africa insolation (precipitation dynamics)	Alternating high – low climate variability	Sustained period of strong climate variability

1010
1011

Figures



1012

1013 **Fig. 1. Archeological and faunal transitions in the Ologesailie basin and location, lithology,**

1014 **and geochronology of the Ologesailie Drilling Project core OLO12-1A. (A) – (C) Locations**

1015 **of Koora basin drill core, Ologesailie, Lainyamok fossil site, and east-to-west faulted topography**

1016 **(cross-section). (D) Ologesailie basin Acheulean technology spanning ~1 Ma to 500 ka;**

1017 **replacement by Middle Stone Age technology ~320 ka; and turnover in the fossil mammalian**

1018 **fauna (6-8), including community-level change in body mass, water dependence, and feeding**

1019 **strategies (table S1). Fossil assemblages dated between ~397 ka and 300 ka recording the faunal**

1020 **turnover are from Ologesailie and Lainyamok (7, 8, 43). The hominin behavioral and faunal**

1021 **transitions in the Ologesailie basin occurred during an erosional hiatus dated ~500 ka to 320 ka.**

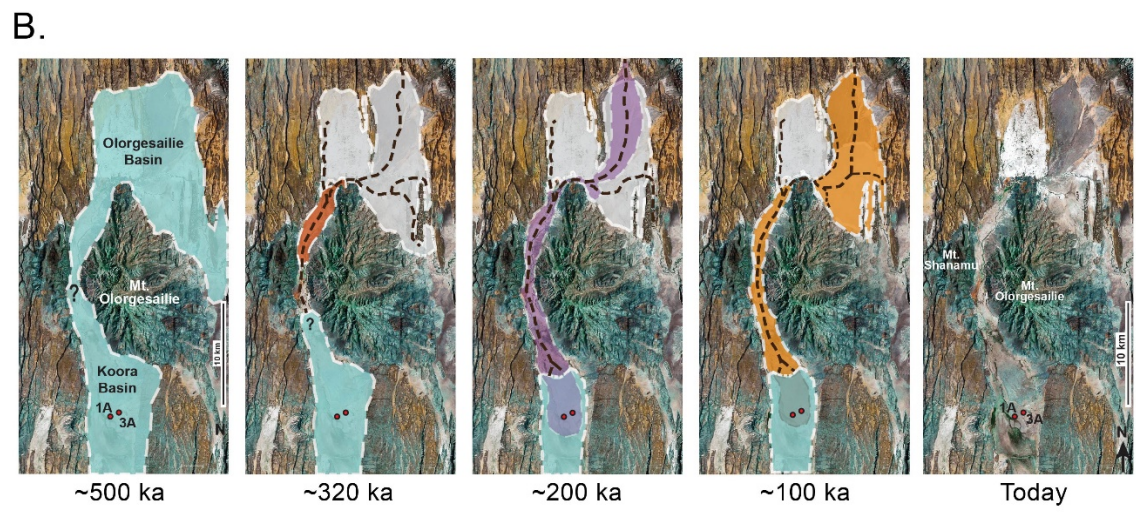
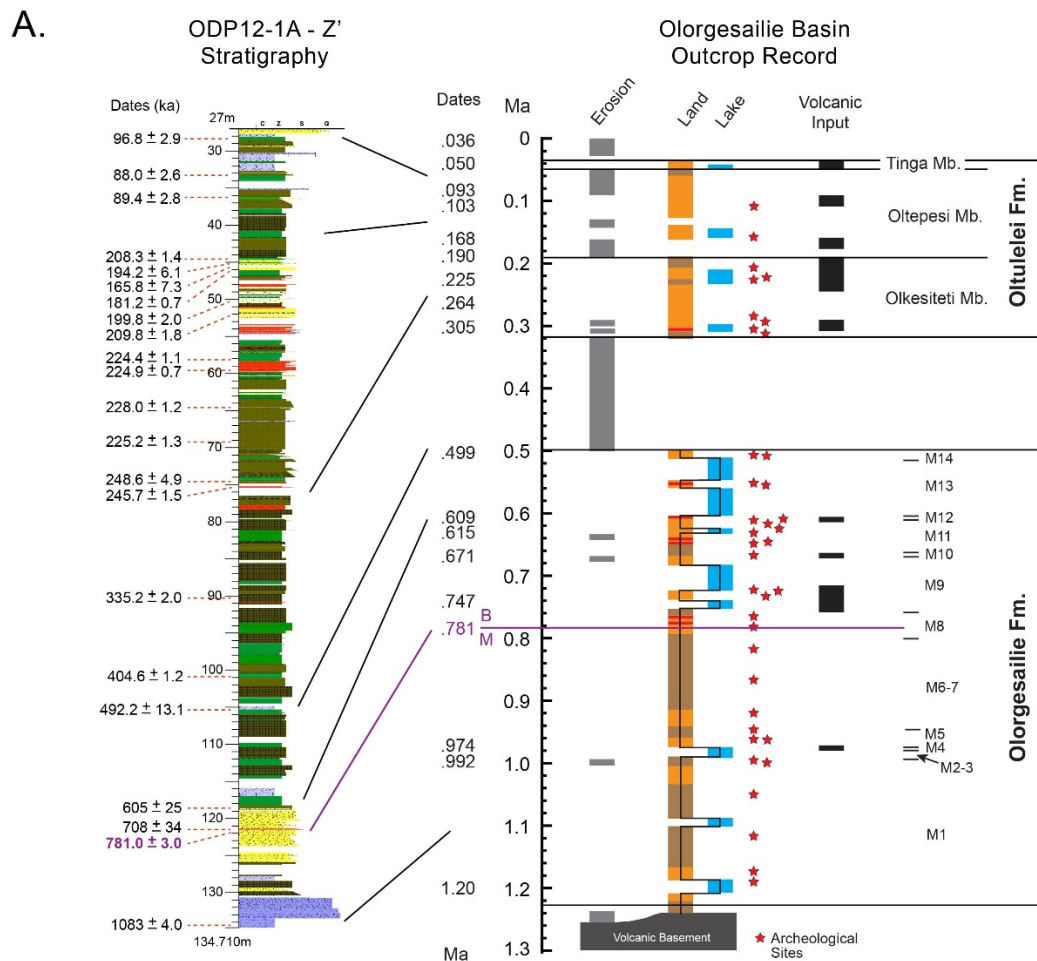
1022 **(Map image: TanDEM-X DEM © DLR; tool images: J.B. Clark, Smithsonian Institution) (E)**

1023 **Koora basin drill core depth (meters below surface), lithological sequence, and age constraints**

1024 **spanning from ~1.084 Ma to ~83.5 ka, based on Bayesian age model (⁴⁰Ar/³⁹Ar ages±1σ and**

1025 Brunhes/Matuyama magnetostratigraphic boundary*) (19). Shaded zone indicates drill core
 1026 lithological record during the hiatus in the Olorgesailie outcrop record. See Fig. 2, fig. S1
 1027 (lithological key), and Materials and Methods.

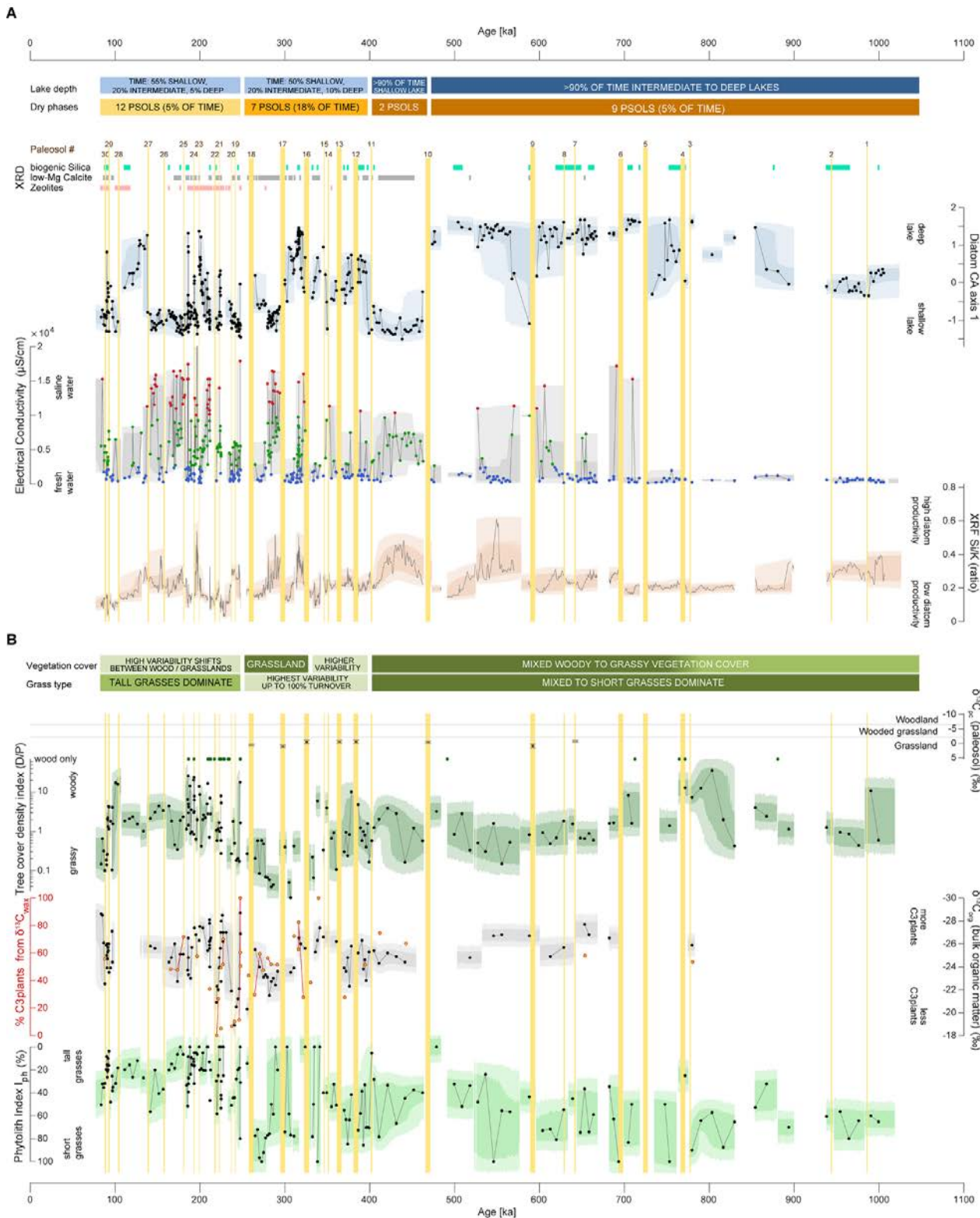
1028



1029
1030

1031 **Fig. 2. Stratigraphic and paleohydrologic relationships between the Koora basin, where the**
1032 **ODP-OLO12-1A drill core was obtained (Fig. 1), and the Olorgesailie basin, where the**
1033 **transitions in Acheulean-MSA behavior and mammalian fauna are recorded. (A)** Correlation
1034 between OLO12-1A z-prime core stratigraphy and the Olorgesailie basin outcrop record, based on
1035 dates in (7, 8, 19). Note the stratigraphic column is corrected for rapid and instantaneous deposits
1036 and thick volcanoclastic layers (red color) and event deposits consequently removed. The overall
1037 z-prime core thickness is therefore lower than that of the recovered core; see ref. 19.
1038 **(B)** Hypothesized reconstruction of basin history and drainage relationships of the Olorgesailie
1039 and Koora basins from 500 ka to present. The sequential maps show the connections between the
1040 two basins, based on sediment correlations and tephra dates, and illustrate increasing
1041 compartmentalization of this part of the southern Kenya rift over the past 500 kyr (34). Note that
1042 this reconstruction is based on the present-day topography and that the spatial extent of the Koora
1043 basin paleolake is approximate. Question marks denote uncertainties in lake extent in the northern
1044 Koora basin. Color code: blue = lake, white = eroding outcrops of the Olorgesailie Fm., red-
1045 orange = major paleosol (base of Olkesiteti Mb., Oltulelei Fm.), purple = major volcanoclastic
1046 influx, (Olkesiteti Mb, Oltulelei Fm.), orange = volcanoclastics plus fluvial siliciclastic sediments
1047 (Oltepesi Mb., Oltulelei Fm.). Red dots in the Koora basin mark the locations of drill cores.

1048
1049



1050

1051

Fig. 3. Paleoenvironmental data from core ODP-OLO12-1A. Colored horizontal bars

1052

summarize intervals of similar paleoenvironmental conditions; darker to lighter colors represent

1053

lower to higher variability intervals. Vertical yellow bars denote paleosols, indicating lake

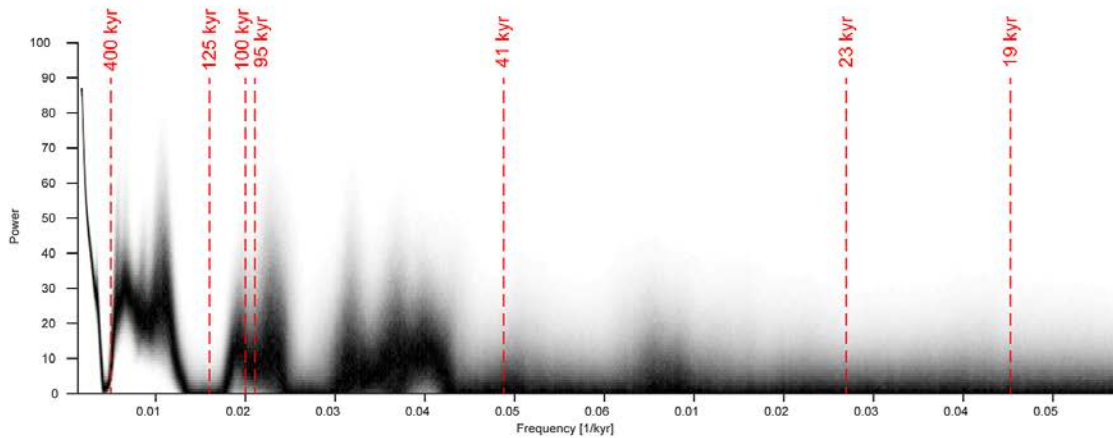
1054

desiccation. (A) Water availability data: X-Ray diffraction (XRD) shows major mineral groups

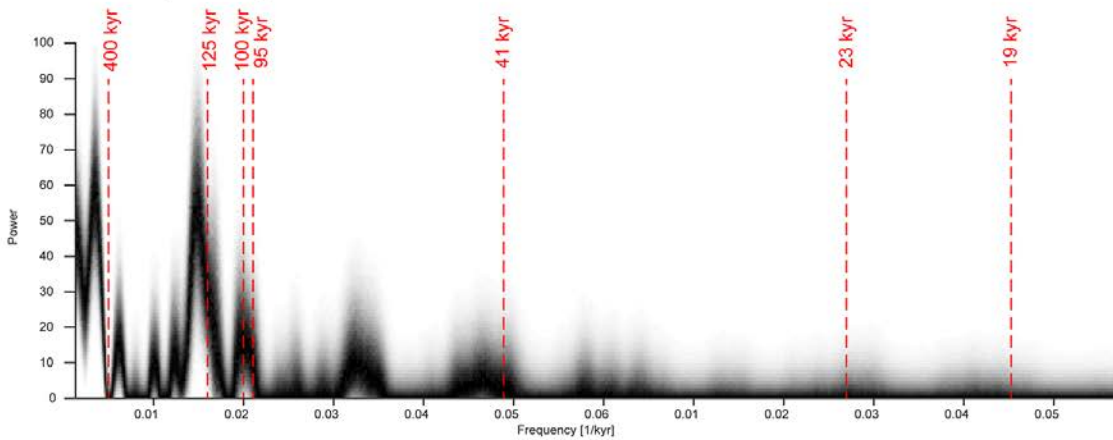
1055 (zeolites: predominantly analcime and phillipsite). Correspondence analysis (CA) scores of
1056 diatom assemblage data indicate fluctuations in lake water depth. Electrical Conductivity (EC) of
1057 paleolake waters are derived from a diatom transfer function (blue=fresh, green=brackish,
1058 red=saline; 2500 $\mu\text{S}/\text{cm}$ assumed limit of potable water for humans). Ratio of silica and
1059 potassium counts from X-Ray fluorescence (XRF) analysis shows five-point moving average;
1060 high (low) values indicate high (low) diatom productivity (text S3) (46). **(B)** Vegetation dynamics
1061 data: Stable carbon isotope values of carbonate nodules ($\delta^{13}\text{C}_{\text{pc}}$) from paleosols; vegetation
1062 classes from (47). Tree cover density index (D/P) of phytolith assemblage data (30): higher values
1063 indicate dense woody cover; green dots denote absence of grass phytoliths. Stable isotope values
1064 of bulk sedimentary organic matter ($\delta^{13}\text{C}_{\text{org}}$; black) and proportion of C_3 vs. C_4 plants from plant
1065 leaf wax isotopes ($\delta^{13}\text{C}_{\text{wax}}$; red). Phytolith index (Iph) from grass phytolith data indicate
1066 proportion of short (Chloridoideae) vs. tall (Panicoideae) grasses (29). All datasets are plotted at
1067 their median age. Dots denote single data points; envelopes reflect 68% (dark) and 95% (light)
1068 confidence intervals (19). Continuity of data and uncertainty envelopes are interrupted at hiatuses,
1069 core gaps, and measurement gaps.

1070
1071

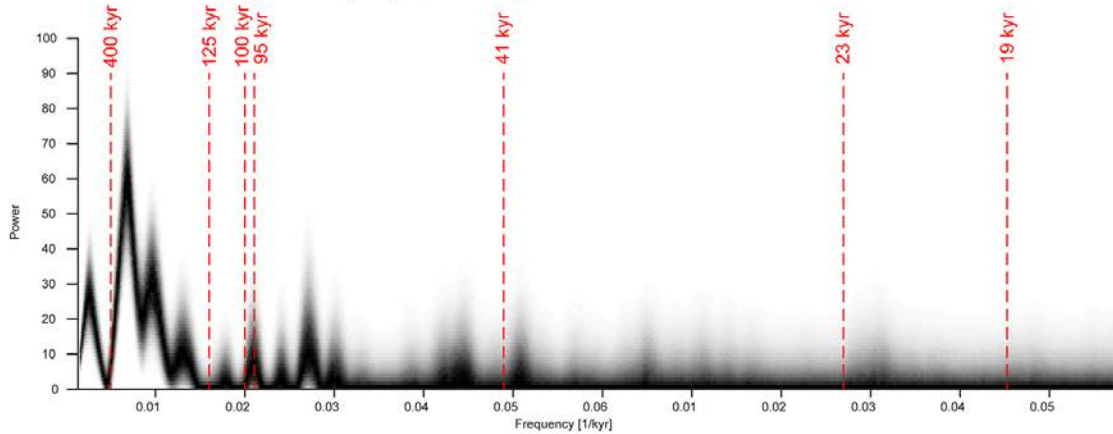
A Diatom CA1 power spectrum stack



B XRF Si/K power spectrum stack



C Tree cover density index (D/P) power spectrum stack



1072

1073

1074

1075

1076

Fig. 4. Time-series (power spectrum) analyses on ODP-OLO12-1A environmental indicator (proxy) records. Lomb-Scargle spectra for (A) the diatom CA1 axis, an indicator for lake depth, (B) the XRF Si/K ratio, an indicator of paleohydrology, and (C) the phytolith D/P index, an indicator of paleovegetation and tree cover. Orbital periods (400, 100, 41, 23-19 kyr) are shown

1077 with red dashed lines. Spectral analysis was used to explore orbital variability within the various
1078 time series, taking into account the uncertainty of the age model (see Materials and Methods).
1079 Darker colors represent spectral powers of the data that are more consistent across the full age
1080 model. Orbital variability is present but subdued in these records: The percentage of total variance
1081 occurring at orbital periods is only 11% in the diatom CA1 record (8% eccentricity, 2% obliquity,
1082 1% precessional periods), 17% in the XRF Si/K time series (8% eccentricity, 7% obliquity, 1%
1083 precessional periods) and 16% in the phytolith D/P tree cover record (9% eccentricity, 3%
1084 obliquity, 4% precessional periods). Records are shown in comparison with orbital cycles in fig.
1085 S4.

1086

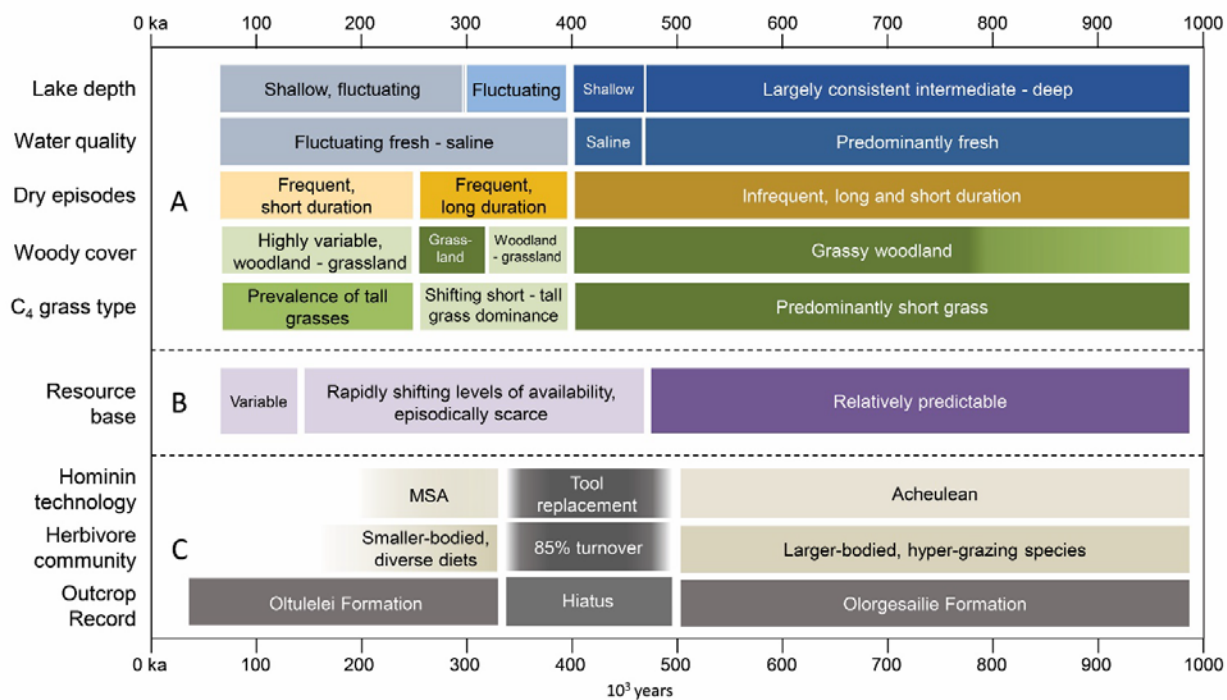


Fig. 5. Transitions in resource dynamics, hominin behavior, and mammalian fauna over time based on the OLO12-1A drill core and Ologesailie outcrop data. (A) Water availability and vegetation dynamics based on Fig. 3 datasets (see text). Darker bars reflect relatively consistent resources, lighter colors more variable resources. Intermediate-to-deep lake conditions ~938 to 830 ka are based on lower-resolution data due to core gaps (data table S4). **(B)** Change in resource base availability and predictability based on the synthesis in (A). The horizontal bars in (A) and (B) describe dominant inferred patterns for each time period of the core; the transitions are not typically abrupt. **(C)** Major transitions in hominin behavior and the herbivore community based on outcrop records of the southern Kenya rift. These transitions took place during the erosional hiatus between 500 and 320 ka. The marked shift from reliable to variable resource landscapes beginning ~400 ka in the adjacent Koora record (Fig. S9) occurred within the interval of the Ologesailie erosional hiatus and the major transitions.

Supplementary Materials for

1109
1110
1111
1112
1113
1114
1115
1116

Increased ecological resource variability during a critical transition in hominin evolution

1109 Richard Potts*, René Dommain, Jessica W. Moerman, Anna K. Behrensmeyer, Alan L. Deino,
1110 Simon Riedl, Emily J. Beverly, Erik T. Brown, Daniel Deocampo, Rahab Kinyanjui,
1111 Rachel Lupien, R. Bernhart Owen, Nathan Rabideaux, James M. Russell, Mona Stockhecke,
1112 Peter deMenocal, J. Tyler Faith, Yannick Garcin, Anders Noren, Jennifer J. Scott,
1113 David Western, Jordon Bright, Jennifer B. Clark, Andrew S. Cohen, C. Brehnin Keller,
1114 John King, Naomi E. Levin, Kristina Brady Shannon, Veronica Muiruri, Robin W. Renaut,
1115 Stephen M. Rucina, Kevin Uno

1116
1117 *correspondence to: pottsr@si.edu
1118

1119 **This PDF file includes:**
1120

1121 materials and methods

1122 fig. S1. Lithological key

1123 fig. S2. Bayesian age model for core ODP-OLO12-1A on the z-prime depth scale

1124 fig. S3. Electrical Conductivity (EC) (n = 476) of paleolake waters derived from a transfer
1125 function approach based on diatom data

1126 fig. S4. Earth's orbital cycles in comparison to key datasets from core ODP-OLO12-1A
1127 fig. S5. Vegetation proxy results for core ODP-OLO12-1A
1128 fig. S6. Interassemblage variability in (A) diatom taxa and (B) phytolith morphotypes, in samples
1129 through the ODP core OLO12-1A, from ~1.084 Ma to ~83 ka
1130 fig. S7. Derived sedimentation rate (in cm/yr) and percentage of volcanic glass based on complete
1131 microscopic sediment composition
1132 fig. S8. Divergent vegetation signals evident in (A) the Magadi basin pollen record (37) and (B)
1133 the ODP-OLO12-1A Koora basin phytolith woody cover density record (D/P index, Fig. 3B) over
1134 the past 600,000 years
1135 fig. S9. Expanded datasets indicating (A) water availability and (B) vegetation dynamics,
1136 covering the critical window between 500 ka and 300 ka, from main text Fig. 3A and 3B.
1137 table S1. Taxonomic composition of Acheulean- and MSA-associated mammalian faunas of the
1138 Olorgesailie basin, categorized by body mass, water-dependence, and feeding strategy based on
1139 functional morphology and modern taxonomic analogues
1140 table S2. Minimum water table depth below exposure surfaces (last column) by stratigraphic
1141 interval between 470.73 ka and 262.91 ka
1142 supplementary text S1. Geochronology and core stratigraphy
1143 supplementary text S2. Terrestrial trace fossils and minimum water table depth
1144 supplementary text S3. Use of Si/K as an indicator of water availability
1145
1146 Supplementary data tables:
1147 data table S3: Diatom taxa percentages on the drilled meters below surface depth scale
1148 data table S4: Diatom CA axis 1 (dimensionless scores), on age model time scale with median
1149 ages and uncertainties (a)

1150 data table S5: Diatom electrical conductivity (EC), on age model time scale with median ages and
1151 uncertainties (a)

1152 data table S6: Phytolith counts and indices on age model scale with median ages and uncertainties
1153 (a)

1154 data table S7: Carbon and oxygen isotope values of pedogenic carbonates samples from Koora
1155 basin core ODP-OLO12-1A, showing isotope data for each sample used to calculate the mean
1156 paleosol $\delta^{13}\text{C}$ value, on meters below surface depth scale (see table S9)

1157 data table S8: Mean pedogenic carbonate carbon and oxygen isotope data for paleosols in Fig. 3B
1158 in Koora basin core ODP-OLO12-1A, on age model scale. Mean values are shown for each
1159 paleosol in Fig. 3B.

1160 data table S9: XRF core scanning for Si/K ratio on age model time scale with median ages and
1161 uncertainties (a)

1162 data table S10: XRD data on age model time scale with median ages and uncertainties (a)

1163 data table S11: $\delta^{13}\text{C}$ -leafwax, percent C_3 leaf waxes on age model time scale with median ages
1164 and uncertainties (a)

1165 data table S12: $\delta^{13}\text{C}$ bulk organic matter on age model time scale with median ages and
1166 uncertainties (a)

1167

1168 References (90-109)

1169

1170 **Supplementary materials and methods**

1171 **Drilling procedure, location, depth, processing, and sampling (R.P., R.D., A.N., A.K.B.)**

1172 Selection of drilling sites within the Koora basin was based on (1) proximity and potential to
1173 capture Ologresailie basin sediments; (2) drainage from Ologresailie into the Koora basin; and (3)
1174 magnetic and seismic reflectance data from 2009-2011 that suggested >10s of meters of sediment

1175 beneath the flat-lying plain above basement lava. Drilling was performed by Drilling and
1176 Prospecting International (DPI) using a truck-mounted PRD Multistar drilling rig with Boart
1177 Longyear HQ3 and HQT tooling for coring (3m cores of 61mm diameter, collected in
1178 polycarbonate liners), and auger and reverse circulation methods for destructive drilling in the
1179 upper 27 meters of the borehole. Drilling operations began on 03 September 2012 and concluded
1180 on 15 September 2012, and generally consisted of a single 14- to 16-hour shift.

1181 Borehole ID: ODP-OLO12-1A. Borehole IGSN: CDR0003AG. Latitude/ Longitude: -1.791,
1182 36.40113. Top elevation: 862 m. Depth to top of cored interval: 27 m. Cored length: 139.1 m.
1183 Total depth: 166.14 m. Core recovery: 94%.

1184 On retrieval, cores were extracted from the drilling tool, cut to sections ≤ 150 cm long, capped,
1185 sealed with tape, and labeled according to standard LacCore facility protocols. Drilling metadata
1186 were captured throughout coring operations and transferred to the LacCore Facility for integration
1187 with all project data sets. At the conclusion of drilling, cores were crated and shipped via truck
1188 and air freight to the LacCore Facility at the University of Minnesota for processing, description,
1189 scanning, subsampling, and permanent curation in the LacCore repository in refrigerated
1190 conditions (4°C).

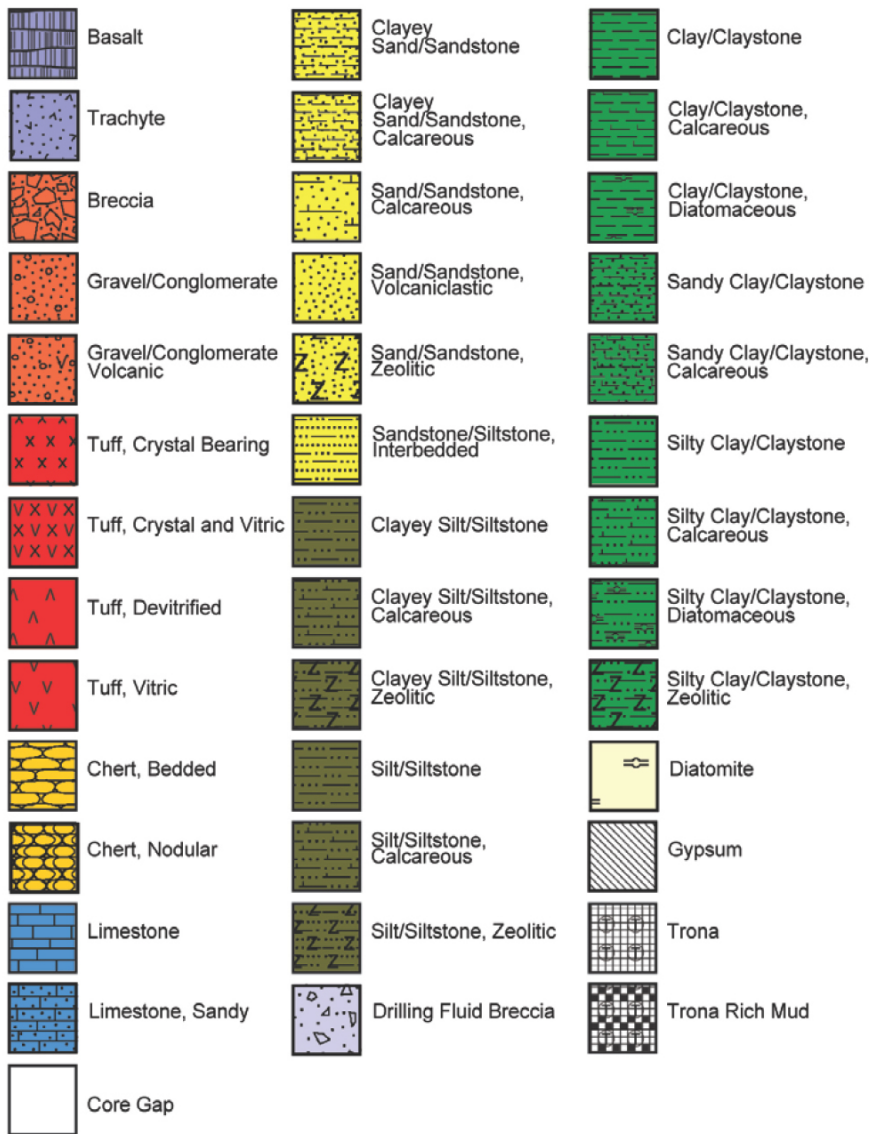
1191 LacCore facility staff passed the cores through a Geotek MSCL-S multisensor core logger for
1192 standard parameters: magnetic susceptibility, gamma density, p-wave velocity, electrical
1193 resistivity, and natural gamma radiation. Project scientists convened at the LacCore facility in
1194 April 2013 for core description and subsampling. Cores were split in half lengthwise with a rock
1195 saw. The archive half of each core was photographed with a Geotek MSCL-CIS optical linescan
1196 camera at 50-micron resolution. Visual lithologic core descriptions were subsequently recorded
1197 on Initial Core Description LacCore software by A.K.B and R.B.O., which also included
1198 petrographic smear slide analysis by R.D. SEM-EDS, and XRD analyses were used as needed for
1199 component identification. Archive halves were subsequently logged on a Geotek MSCL-XYZ

1200 split-core multisensor logger for high-resolution magnetic susceptibility and color reflectance
1201 spectrophotometry, and later scanned on an ITRAX XRF Core Scanner for elemental distributions
1202 and X-radiographic imaging (see below). The working half of each core was subsampled for the
1203 discrete analyses described below. For the entire core, we used a sampling interval of 48 cm down
1204 to volcanic basement rock, followed by further subsampling to examine diatom assemblages at
1205 finer resolution and to attempt to fill in gaps in isotopic and other data analyses.

1206 **Lithological description (A.K.B., R.B.O., R.D.)**

1207 Sediments in the core are relatively fine-grained and include input from both siliciclastic and
1208 volcanoclastic source areas as well as lacustrine biosilica. Based on macroscopic and microscopic
1209 core description methods, there are 345 recognizable lithological units in core ODP-OLO12-1A
1210 above the basal trachyte. In terms of proportion of total thickness, these units consist of
1211 siliciclastic silt (44%), clay (20%), sand (14%) and gravel (4%), mixed with varying amounts of
1212 diatomite, volcanic glass, calcium carbonate, and zeolite. Relatively pure tephras make up about
1213 17% of the core. Approximately half of the silt-grade sediment is diatomaceous, with pure
1214 diatomites comprising only ~1% by thickness. Bedding structures indicating sub-aqueous
1215 deposition include well-defined, mm-to-cm scale horizontal laminae, ripple and wavy lamination,
1216 burrows, and contorted bedding indicating post-depositional slumping. Subaerial structures
1217 include desiccation cracks, root traces and burrows, pedogenic features such as peds, slickensides,
1218 and erosional scours. Contacts between units range from gradational to sharp, even to irregular.
1219 The sedimentary evidence throughout much of the core records cycles in which lacustrine
1220 deposition was followed by lake regression and modification of the lacustrine sediments by
1221 subaerial surface processes. The lithological key (fig. S1) indicates primary sediment composition
1222 and does not incorporate pedogenic modification of the sediments. Sedimentation rates increased
1223 with periodic volcanoclastic input to the Koora basin after 400 ka, and especially after ~270 ka
1224 (19) when there is a corresponding decrease in estimated paleosol duration.

Key to lithologic symbols



1225

1226 **Fig. S1.**

1227 **Lithological key for Figs. 1E and 2A.** White indicates missing core (i.e. no recovery). Key from

1228 ref. 20 and based on standardized lithological symbols for core description

1229 <https://csdco.umn.edu/resources/software/psicat>.

1230

1231 **Table S1.**

1232 **Taxonomic composition of Acheulean- and MSA-associated mammalian faunas of the**

1233 **Ologesailie basin, categorized by body mass, water-dependence, and feeding strategy based**

1234 **on functional morphology and modern taxonomic analogues. (A)** Ecological characteristics

1235 for each taxon. **(B)** Summary counts of taxa attributed to ecological categories as shown in Fig.

1236 1D pie charts comparing Oltulelei and Ologesailie Fm. faunas.

1237 **A**

Family	Ologesailie Fm. Acheulean-associated fauna	Oltulelei Fm. MSA-associated fauna	Common name	Feeding strategy (diet) ¹	Body mass estimated average (kg)	Body size class ²	Water Dependence ³	References ecology/physiology
Bovidae		<i>Madoqua</i> sp.	dik dik	B	6	1b	N	25,90
		<i>Antidorcas marsupialis</i>	springbok	M	40	2	L	90,91
		<i>Gazella</i> sp.	gazelles	G	40	2	N/L	90,91
		<i>Gazella thomsoni</i>	Thompson gazelle	G	25	2	L	25,90
		<i>Aepyceros</i> sp.	impala	M	60	2	H	90,92
		<i>Megalotragus</i> sp.	large extinct	G	400	4	Y ⁴	
		Alcelaphin size 3a cf. <i>Alcelaphus</i>	Alcelaphin/hartebeest	G	175	3a	H	25,90
		<i>Connochaetes</i> sp.	wildebeest	G	250	3b	H	25,90
		<i>Damaliscus hypsodon</i>	extinct blesbok	G	70	2	Y ⁴	
		<i>Oryx</i> cf. <i>O. beisa</i> - Hippotragin oryx size	Beisa oryx	G	200	3a	L	90,91
		Hippotragin - roan size	roan antelope	G	280	3b	? ⁵	
		<i>Taurotragus</i> sp.	eland	B	600	4	N	90
		<i>Taurotragus oryx</i>	common eland	B	600	4	N	90
		<i>Tragelaphus scriptus</i>	bushbuck	M	50	2	L	90
Suidae		<i>Tragelaphus strepsiceros</i>	greater kudu	B	250	3b	L	90
		<i>Tragelaphus</i> cf. <i>T. imberbis</i>	lesser kudu	B	80	3a	N	25,90
		<i>Syncerus (Pelorovis)</i> cf. <i>S. antiquus</i>	extinct wild buffalo	G	900	5	Y ⁴	
		<i>Kobus</i> cf. <i>K. kob</i>	kob	G	80	3a	H	90
		<i>Redunca</i> sp.	reedbuck	G	50	2	Y	93
		<i>Giraffa</i> sp.	giraffe	B	1500	5	L	25,90,92
		<i>Metridiochoerus</i> cf. <i>M. hopwoodi</i>	extinct giant warthog genus	G	250	3b	Y ⁴	
		<i>Metridiochoerus</i> cf. <i>M. compactus</i>	extinct giant warthog genus	G	150	3a	Y ⁴	
		<i>Kolpochoerus majus</i>	extinct forest/riverhog genus	G/M	120	3a	Y ⁴	
		<i>Phacochoerus</i> sp.	warthog	G	100	2	Y	25,90
Hippopotamidae	<i>Hippopotamus</i> cf. <i>H. gorgops</i>	<i>Phacochoerus</i> sp.	warthog	G	100	2	Y	25,90
		<i>Hippopotamus</i> cf. <i>H. amphibious</i>	extinct hippopotamus	G	3000	6	Y ⁶	
Equidae		<i>Equus</i> cf. <i>E. quagga</i>	hippopotamus	G	1500	5	H	90
		<i>Equus</i> cf. <i>E. grevyi</i>	Plains zebra	G	250	3b	H	90
		<i>Equus oldowayensis</i>	Grevy's zebra	G	400	4	L	90,92
		<i>Eurygnathohippus</i> sp.	extinct zebra/horse	G	450	4	Y ⁶	
		<i>Equus</i> aff. <i>E. capensis</i>	extinct horse	G	200	3a	Y ⁶	
Rhinocerotidae	<i>Ceratotherium simum</i>		white rhino	G	2500	5	H	90
	<i>Diceros bicornis</i>		black rhino	G	1100	5	H	90
Elephantidae	<i>Diceros bicornis</i>	<i>Diceros bicornis</i>	black rhino	G	1100	5	H	90
	<i>Palaeoaloxodon (Elephas) recki</i>		extinct elephant	G	8000	6	H ⁶	
Rodentia		<i>Loxodonta africana</i>	savanna elephant	M	4500	6	H	25,90
		<i>Hystrix cristata</i>	crested porcupine	M	15	1c	N	92
		<i>Pedetes</i> sp.	springhare	G	3	1b	N	94
Primates		<i>Lepus</i> sp.	hare	G	2	1b	N	94
	<i>Theropithecus oswaldi</i>		extinct gelada monkey	G	200	3	Y ⁶	

1. Diet: G=grazer B=browser M=mixed grazer/browser

2. Body size class: 0: indet 1: <23kg (1a: <1kg; 1b: 1-10kg; 1c: 10-23kg) 2: 23-113kg 3: 113-340kg (3a: Topi size; 3b: Wildebeest/zebra size) 4: 340-900kg 5: 900-2700kg 6: >2700kg

3. Water dependence: H=high L=low N=none Y=high or low ?=unknown

4. As a ruminant grazer, classified as water dependent (low or high).

5. Cannot classify indeterminate hippotragin; *Hippotragus* is highly water dependent but not *Oryx*.

6. Family/tribe-level physiological analogues

1238

B

Geological Unit	Ecological characteristic					
	Body mass category					
	Class 6	Class 5	Class 4	Class 3	Class 2	Class 1
Oltulelei Fm.	1	2	2	5	4	4
Ologesailie Fm.	2	4	4	8	5	0

	Water dependent?				
	Yes	High	Low	No	Unknown
Oltulelei Fm.	3	4	4	6	1
Ologesailie Fm.	11	7	4	1	0

	Feeding strategy			
	Megagrazer	Grazer	Mixed feeder	Browser
Oltulelei Fm.	2	9	3	4
Ologesailie Fm.	5	14	2	2

1239

1240

1241

1242

Supplementary Text S1. Geochronology and core stratigraphy

1243

⁴⁰Ar-³⁹Ar geochronology (A.L.D.) – Radiometric age control of the core was established by laser incremental heating ⁴⁰Ar/³⁹Ar dating of individual K-feldspar phenocrysts, extracted mainly from pumice lapilli from tephra horizons sampled opportunistically throughout the depth of the core, and from the basal trachyte flow. In total, 1579 incremental heating steps on 294 phenocrysts from 23 samples were analyzed. Based on observations of core lithostratigraphy and smear slide analysis, these samples date 22 distinct tephrostratigraphic units, representing typically discrete volcanic events, but in some cases recording tightly spaced, effectively continuous pulses of pyroclastic volcanism (19).

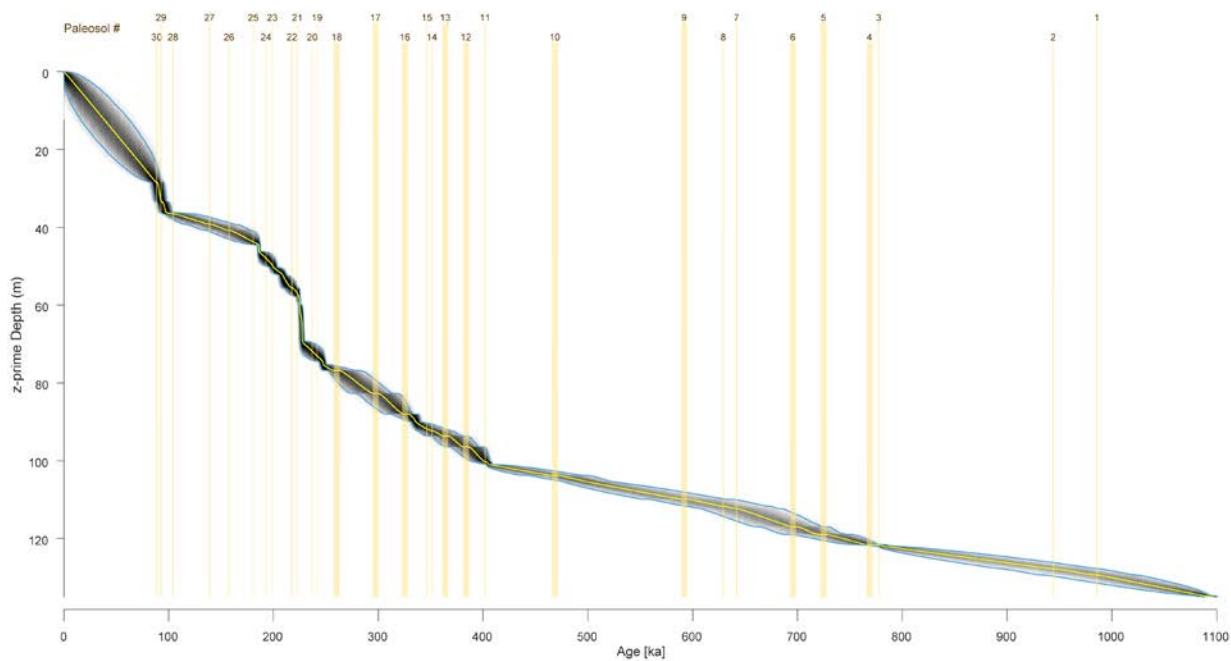
1251

Magnetostratigraphy (J.K., C.W.H.) - A total of 21 discrete cube samples were taken between 152-162 MBS for paleomagnetic analyses in an attempt to identify the Brunhes/Matuyama Boundary (BMB, 0.781 Ma) (95). The samples were analyzed using a 2-G \square Enterprises small-access cryogenic magnetometer with an in-line alternating field (AF) demagnetization coil in the Paleomagnetism Laboratory at the Graduate School of Oceanography at the University of Rhode Island. The initial natural remanent magnetization (NRM) was measured and then the samples

1256

1257 were subjected to 21 AF demagnetization and measurement steps starting at 2.5 mT and ending at
1258 100 mT (the field was increased by 5 mT between 5 mT and 100 mT) in order to remove any
1259 unstable, viscous remanent magnetizations. Following measurement, the characteristic remanent
1260 magnetization (ChRM) declination and inclination values (96) were calculated using the
1261 Demagnetization Analysis In Excel (DAIE) tool of Sagnotti (97). In order to calculate the ChRM,
1262 we selected between 6-11 demagnetization steps between 5-80 mT and a least-squares fit was
1263 made to the selected data points. The fit was not anchored to the origin of the Zijderveld plot (98)
1264 since the ChRMs generally trended towards the origin without forcing and we felt the unanchored
1265 option gave a better representation of the data quality demonstrated by the maximum angular
1266 deviation (MAD) calculated within the DAIE tool. The criteria for a “quality” ChRM value was
1267 that it be calculated from at least 3 consecutive demagnetization steps and the MAD values were
1268 less than 15° (99). The ChRM declination, inclination, and MAD values were plotted versus depth
1269 in order to identify any possible reversal boundaries. The MAD values are all less than 10° (all
1270 but 3 are <7°) and, considered with the fact that a minimum of 6 demagnetization steps were used
1271 in the calculation of the ChRM, indicate that all of the samples produced quality ChRM
1272 directions. After ruling out declination changes related to core section breaks and potential
1273 coring-induced rotation, we identified a reversal boundary between 153.08-153.15 MBS. This
1274 reversal is characterized by an approximately 160° change in declination between the sample at
1275 153.15 MBS and the 2 samples immediately above it (153.03 and 153.08 MBS). Considering the
1276 stratigraphic position of this reversal and other age constraints, we suggest that this reversal is the
1277 Brunhes-Matuyama Boundary (0.781 Ma).

1278



1279

1280 **Fig. S2.**

1281 **Bayesian age model for core OLO12-1A on the z-prime depth scale, (compressed depth scale**

1282 **corrected for rapid deposition) (19).** Yellow line is median age, grey area represents age

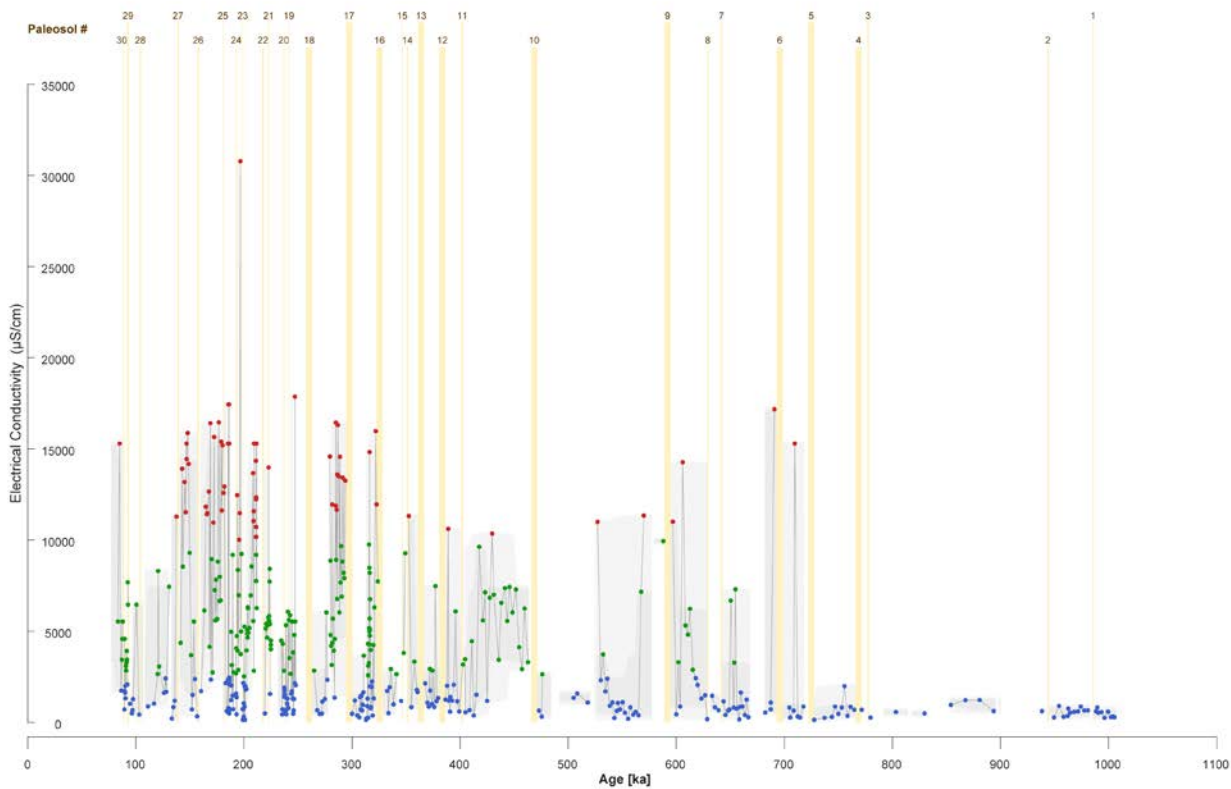
1283 uncertainty and the blue lines mark the 95% confidence intervals. The age model is calculated at a

1284 vertical resolution of one centimeter. Vertical yellow bars represent paleosols and bar thickness

1285 indicates duration of stagnant phases. Periods of non-deposition (i.e., soil formation) are taken

1286 into account in the age model and represented by a slope of zero in the age model

1287 trajectory. Details on the age model are in (19).



1288

1289 **Fig. S3.**

1290 **Electrical Conductivity (EC) ($n = 476$) of paleolake waters derived from a transfer function**
 1291 **approach based on diatom data (see main text Materials and Methods).** Blue, green, and red
 1292 dots indicate fresh, brackish and saline conditions respectively ($2500 \mu\text{S}/\text{cm}$ assumed as the limit
 1293 of potable water for humans) (*100*). Extensive consumption of water values over $10000 \mu\text{S}/\text{cm}$ is
 1294 harmful to various mammal species (*91*). This figure exemplifies our approach of employing drill
 1295 core data (in this case from diatom samples) to derive water salinity (EC), which is used to infer
 1296 water potability, an aspect of landscape resource variability that affected mammalian, including
 1297 hominin, adaptations.

1298

1299 **Supplementary Text S2. Terrestrial trace fossils and minimum water table depth (J.J.S.)**

1300 Terrestrial trace fossils were identified by comparison to modern trace fossils produced in Africa
1301 by termites and other air-breathing taxa (e.g., ants, beetles, spiders) and published examples from
1302 the rock record of Africa (101-106). Diagnostic ichnotaxabases for termite traces include spreiten-
1303 like and meniscate tunnel backfill with sediment aggregates, meniscate-backfilled horizons (i.e.
1304 plates), as well as large excavated nests with sharp boundaries and active and/or passive fill with
1305 sediment aggregates and brecciated host material. Other terrestrial trace fossils not possible to
1306 attribute to particular producers or ichnotaxa were distinguished by sharp boundaries; passive
1307 brecciated fill and/or meniscate backfill; rounded margins and/or circular shape. Some have
1308 sediment fill different from that of host material and the same as pedogenically modified sediment
1309 within the stratigraphic unit. Meniscate backfill with sediment aggregates was considered to be
1310 diagnostic for terrestrial traces in cases where burrows were associated with other features (i.e.,
1311 vertical fracture networks) passively filled by brecciated sediment.

1312 The minimum water table depth below each of the exposure surfaces (table S2) was determined as
1313 the depth of terrestrial bioturbation observed below the top of the overlying paleosol (exposure
1314 surface, as identified by other characteristics, e.g., ped structure). Color, grain-size, and lithology
1315 of the burrow fill were used to identify the associated paleosol top in cases where the traces
1316 crosscut more than one exposure surface. The focus of this study was the stratigraphic interval
1317 with greatest abundance of termite bioturbation, indicating extreme fluctuations in lake-
1318 level/base-level/water-table depth in the OLO12-1A core. This interval was from 139.95 to
1319 107.07 mbs, which encompasses paleosol #10 to paleosol #18.

1320 Terrestrial bioturbation extends to as much as 5.18 m below the top of the corresponding
1321 overlying paleosol (e.g., paleosol #18; table S2), which represents the land surface from which the
1322 burrows originated. In all cases in the OLO12-1A core, the deepest terrestrial traces present
1323 within each interval are attributed to termites. Although there is some variability in the depth of

1324 bioturbation between intervals, in almost all cases bioturbation crosscuts nearly the full thickness
1325 of the interval (from 74% to 96%), and extends up to as much as 2.91 m below the paleosol
1326 bottom depth (e.g., paleosol #18 bottom depth: 109.66 mbs; trace fossil bottom depth: 112.57
1327 mbs). The interval capped by paleosol #13 is an anomaly in the pattern, with only 49% of the total
1328 depth of the sedimentary interval bioturbated by termite traces. This may be due to an artificial
1329 representation of the values for this interval, as core disturbance in section OLO12-1A-67Q-2-A
1330 did not allow for detailed observation.

1331

1332

1333 **Table S2.**
 1334 **Minimum water table depth below exposure surfaces (last column) by stratigraphic interval**
 1335 **between 470.73 ka and 262.91 ka, represented by the depth to deepest terrestrial trace fossil**
 1336 **below paleosol top within the core. See supplementary text S2.**

1337

Paleosol #	Age (ka)	Estimated duration (y)	Paleosol top depth (mbs)	Deepest terrestrial trace in interval (mbs)	Thickness of interval (m)	Minimum water table depth in interval (m)
18	262.91	5000	107.39	112.57	6.09	5.18
17	299.82	5000	113.48	118.21	5.35	4.73
16	328.93	5000	118.83	123.97	5.63	5.15*
15	346.94	250	122.64	—	—	—
14	352.42	750	123.13	—	—	—
13	367.21	5000	124.46	125.87	2.88	1.41**
12	386.72	5000	127.34	131	3.83	3.66
11	402.86	750	131.17	133.77	3.51	2.6
10	470.73	5000	134.67	139.37	6.21	4.7

1338 **Supplementary Text S3. Use of Si/K as an indicator of water availability (M.S., E.T.B.)**

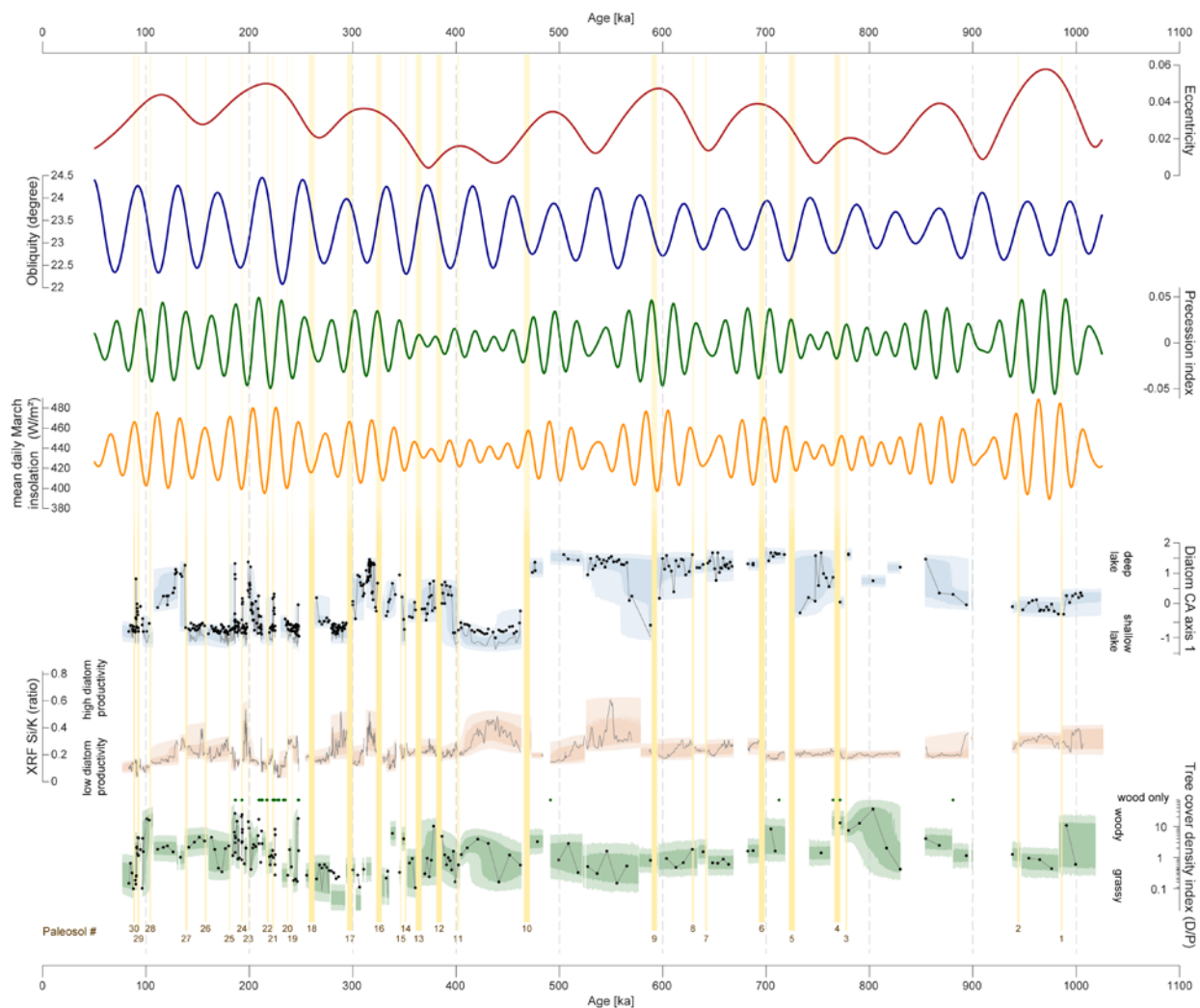
1339 Variations in the biogenic silica content of lacustrine sedimentary archives are frequently
1340 interpreted as records of changing diatom productivity, and of lake productivity more
1341 generally. However, in highly alkaline saline waters such as Na_2CO_3 brines, diatoms are subject
1342 to dissolution so sedimentary records can also reflect water composition (107). In saline systems
1343 variations in biogenic silica can be used as proxy of changes in paleosalinity with enhanced
1344 preservation at times of fresher waters.

1345 Biogenic silica analyses by classic wet chemical methods are labor intensive and time consuming.
1346 Recently XRF scanning techniques have been utilized to provide a rapid and non-destructive
1347 approach to obtain high-resolution records that reflect changing BSi contents of lake sediment. In
1348 order to minimize Si variation due to dilution by biogenic material or carbonate minerals, XRF
1349 data are frequently reported as Si/Ti (108). Ti often serves as a proxy for silicate mineral content
1350 because XRF Al datasets are noisy due to the weak fluorescence from this light element. In the
1351 case of ODP-OLO12 drill cores, we found a good correspondence between XRF Si/K ratios and
1352 diatom counts, and determined that potassium is a better proxy for silicate minerals than Ti. ODP-
1353 OLO12 sediments are rich in volcanoclastic materials, and the Ti content of bulk silicates varies
1354 as a function of enrichment of sedimentary heavy minerals.

1355 In general, higher Si/K ratios reflect lower salinity in ODP sediments. We note that Si/K can also
1356 be impacted by biogenic silica from other autochthonous sources (e.g., chrysophytes and sponges)
1357 and biogenic and non-biogenic allochthonous sources (e.g. grass phytoliths and quartz). However,
1358 the overall strong correspondence between Si/K and diatom counts indicates that diatom contents
1359 are the major source of variability in sedimentary Si content and gives us confidence in this high-
1360 resolution data set.

1361

1362



1363

1364 **Fig. S4.**

1365 **Earth's orbital cycles in comparison to key data sets from core ODP-OLO12-1A.** Variation

1366 in orbital cycles of the past 1 Ma are shown in the top rows (109). Curves show orbital

1367 eccentricity, obliquity (tilt) and precession, as well as resulting mean daily insolation for March at

1368 the latitude of the drilling location (1.8°S). Lower part shows selected paleoenvironmental data

1369 sets (diatom CA 1 axis indicating changes in lake depth, Si/K ratio indicating diatom productivity,

1370 phytolith D/P index indicating tree cover). Spectral analyses of these three indicator data sets

1371 shown in Fig. 4. Vertical yellow bars denote paleosols shown centered on their median ages.

1372

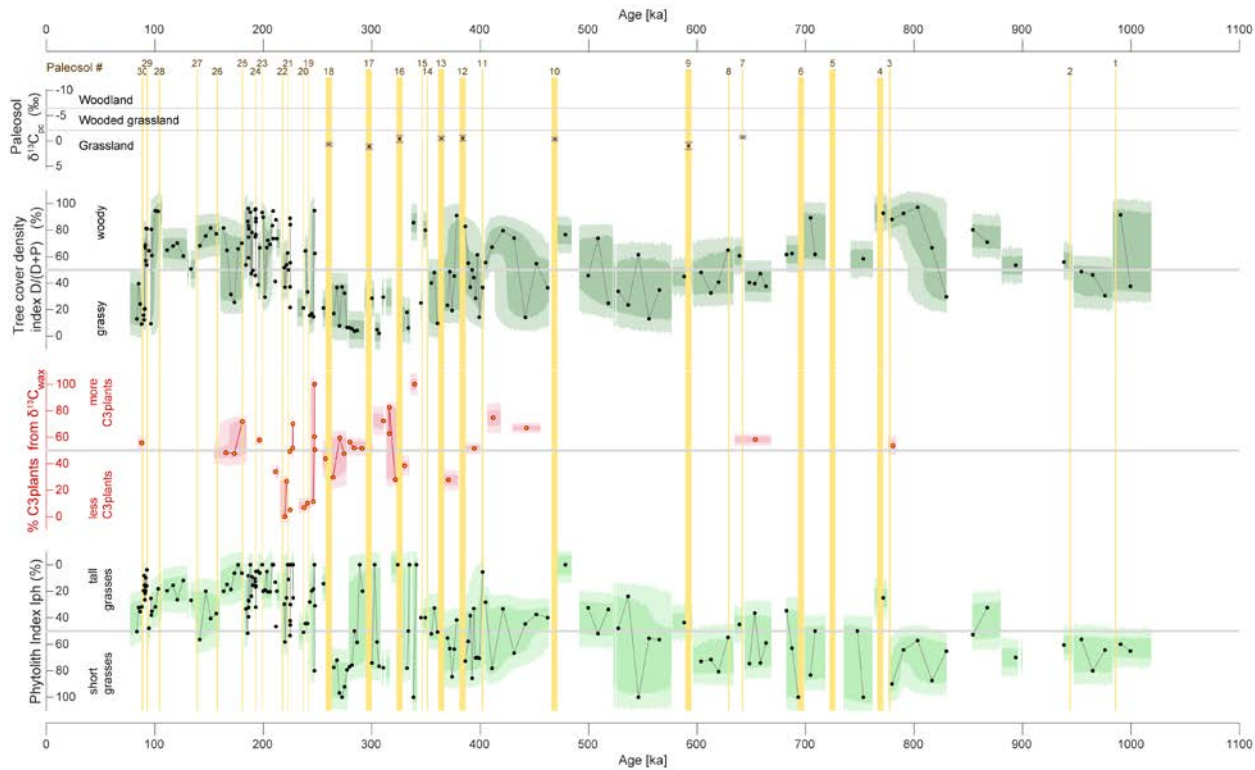
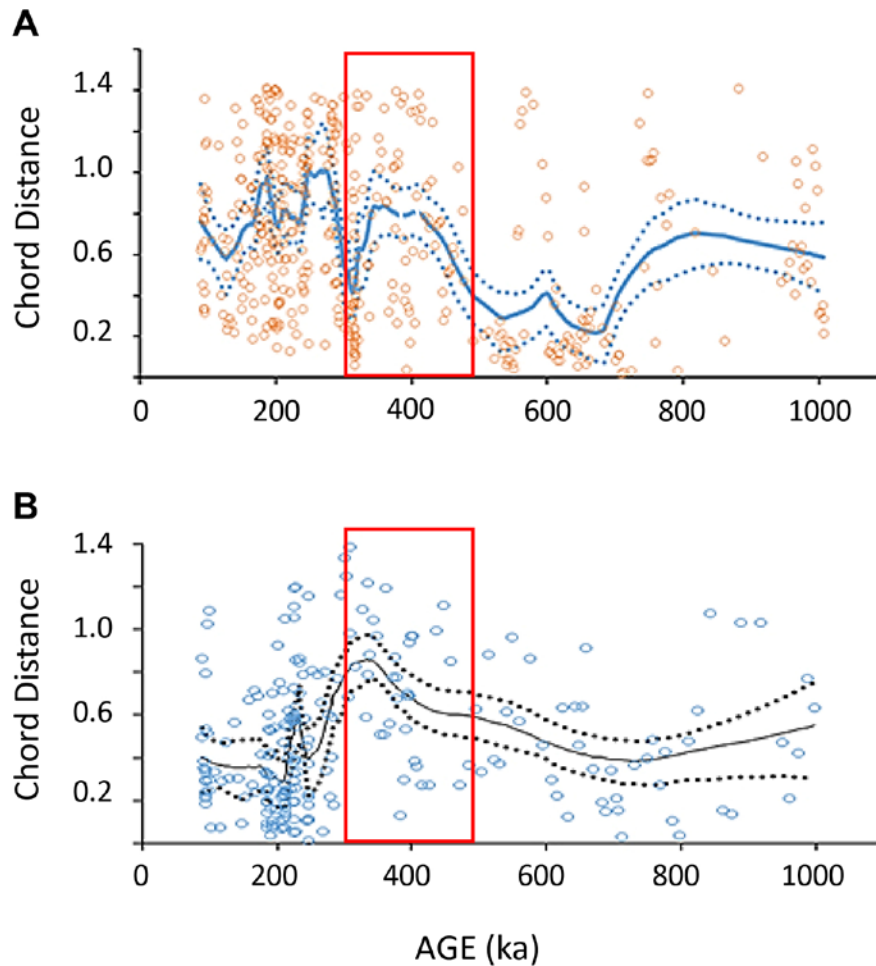


Fig. S5.

Vegetation proxy results for core ODP-OLO12-1A. Comparison between pedogenic carbonate $\delta^{13}\text{C}_{\text{pc}}$ data, an alternative phytolith tree cover index, leaf wax $\delta^{13}\text{C}_{\text{wax}}$, and the phytolith Iph index. Stable carbon isotope values of carbonate nodules ($\delta^{13}\text{C}_{\text{pc}}$) from paleosols ($n = 8$); vegetation classes from (47). The alternative phytolith tree cover index is based on equation $D/(D+P)*100$ and the same phytolith assemblage data ($n = 218$) as for the conventional D/P index shown in Fig. 3B. The alternative calculation integrates samples in which only wood phytoliths were present; higher values indicate denser woody cover. This percentage presentation is used to facilitate comparison with other vegetation signals. We note, however, that the percentage data are not reflecting the actual proportion of woody cover in a landscape and advise to use the conventional phytolith D/P index (Fig. 3B) which is widely used. Stable carbon isotope data of higher plant leaf waxes ($\delta^{13}\text{C}_{\text{wax}}$, $n = 37$) indicate the relative amount of C_3 vs. C_4 plants (see main text Materials and Methods). Phytolith index (Iph) from grass phytolith data indicate proportion of short (Chloridoideae) vs. tall (Panicoideae) grasses ($n = 183$) (29). All data sets are plotted at

1389 their corresponding median age. Dots denote single data points; lines connect single data points;
1390 envelopes reflect 68% (dark) and 95% (light) confidence intervals in the reconstructions, based on
1391 analytical and age model errors (19). Continuity of the data and the uncertainty envelopes are
1392 interrupted at hiatuses, non-recovery intervals, and proxy measurement gaps. Vertical yellow bars
1393 denote paleosols shown centered on their median ages.

1394



1395

1396 **Fig. S6.**

1397 **Interassemblage variability in diatom taxa and phytolith morphotypes in samples through**

1398 **the ODP core OLO12-1A, from ~1.084 Ma to ~90 ka.** Chord distances (open circles) indicate

1399 change in assemblage composition through the sequence. High values represent more turnover;

1400 low values represent less turnover between stratigraphically adjacent assemblages. LOESS

1401 regression of chord distances minimizes variability between assemblages in order to highlight

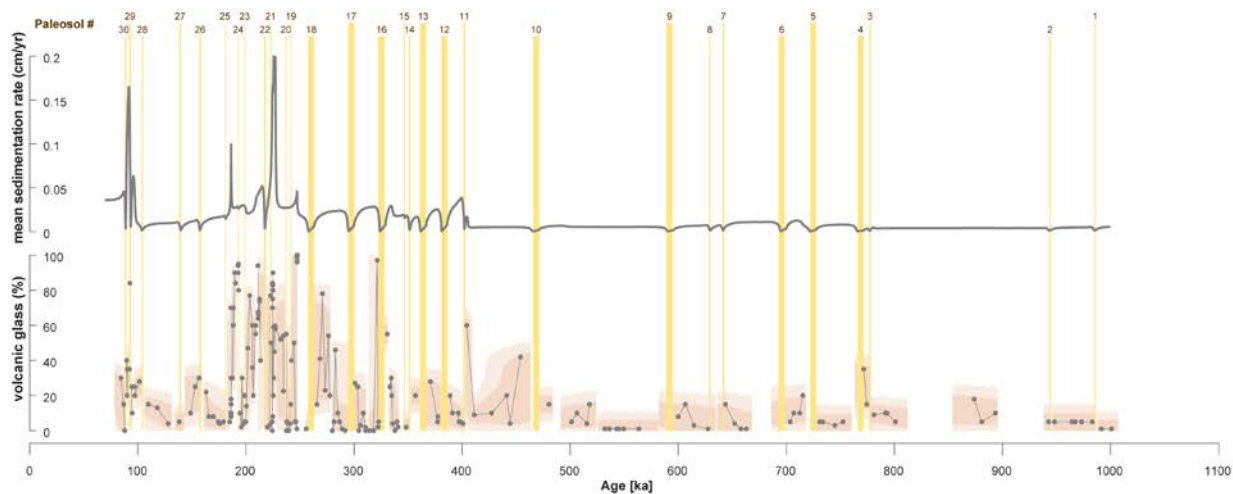
1402 longer-term trends (dashed lines = 95% CI). Red rectangle indicates the window of evolutionary

1403 transition, 500-320 ka. (A) For diatoms, interassemblage taxonomic variability rises above older

1404 regression values between ~425 and ~350 ka, during the interval when we infer the faunal

1405 turnover and the Acheulean-MSA transition occurred. Overall, interassemblage variability

1406 exhibits strong, rapid oscillations throughout the period from ~425 to 90 ka. **(B)** For phytoliths,
1407 interassemblage variability spikes between ~400 and ~350-300 ka, coinciding with the shifts in
1408 hominin and faunal adaptations, after which phytolith assemblages exhibit greater stability.
1409



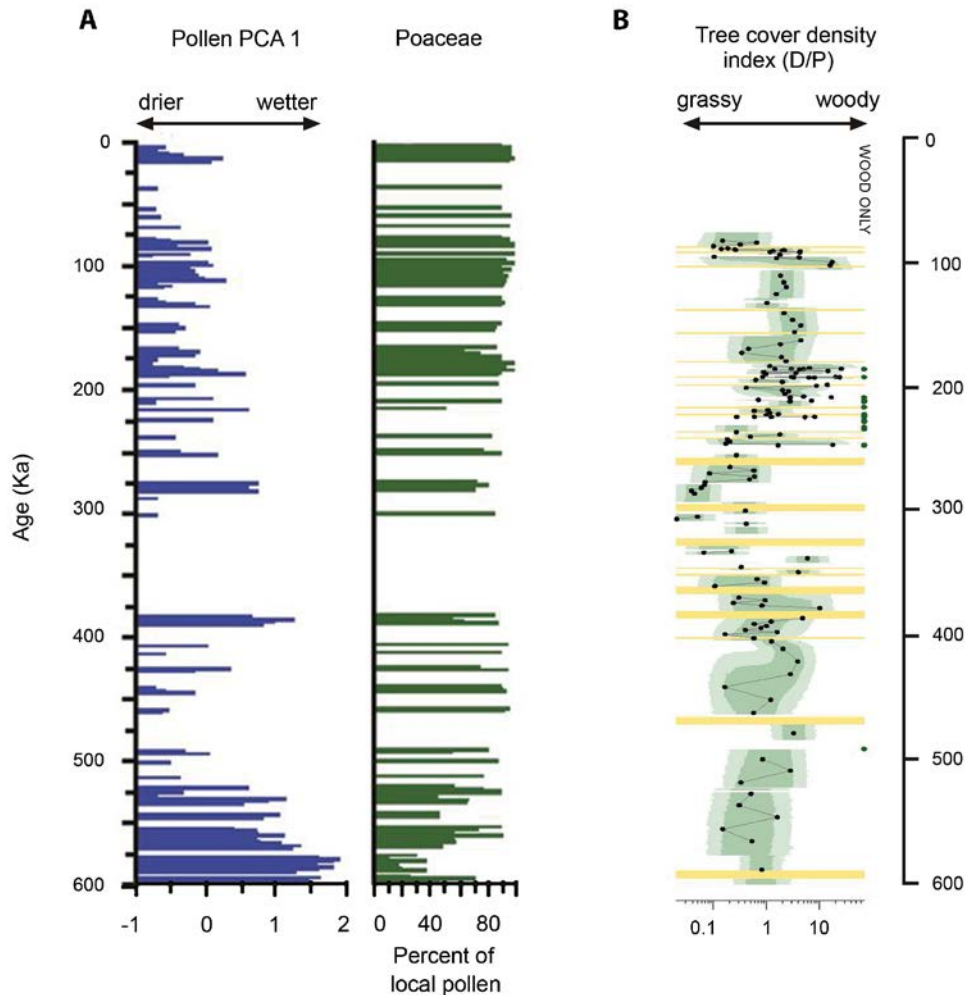
1410

1411

1412 **Fig. S7.**

1413 **Derived sedimentation rate (in cm/yr) and percentage of volcanic glass based on complete**
1414 **microscopic sediment composition.** Sedimentation rate is derived from the median age output of
1415 the Bayesian age model and the z-prime depth scale (19). Vertical yellow bars represent
1416 paleosols; bar thickness represents the duration of stagnant phases.

1417



1418

1419 **Fig. S8.**

1420 **Divergent vegetation signals evident in adjacent basins of the southern Kenya rift over the**

1421 **past 600,000 years. (A)** Drill core data from the MAG14-2A Magadi basin pollen record (37),

1422 and **(B)** the ODP-OLO12-1A Koora basin phytolith woody cover density record (D/P index, Fig.

1423 3B). Magadi pollen PCA 1 is interpreted to reflect an overall trend toward drier climate

1424 (progressive aridification [ref. 37]) from ~575 ka to ~50 ka. Percentage grass taxa (Poaceae)

1425 remains high throughout this interval of the Magadi record, but rises dramatically over time

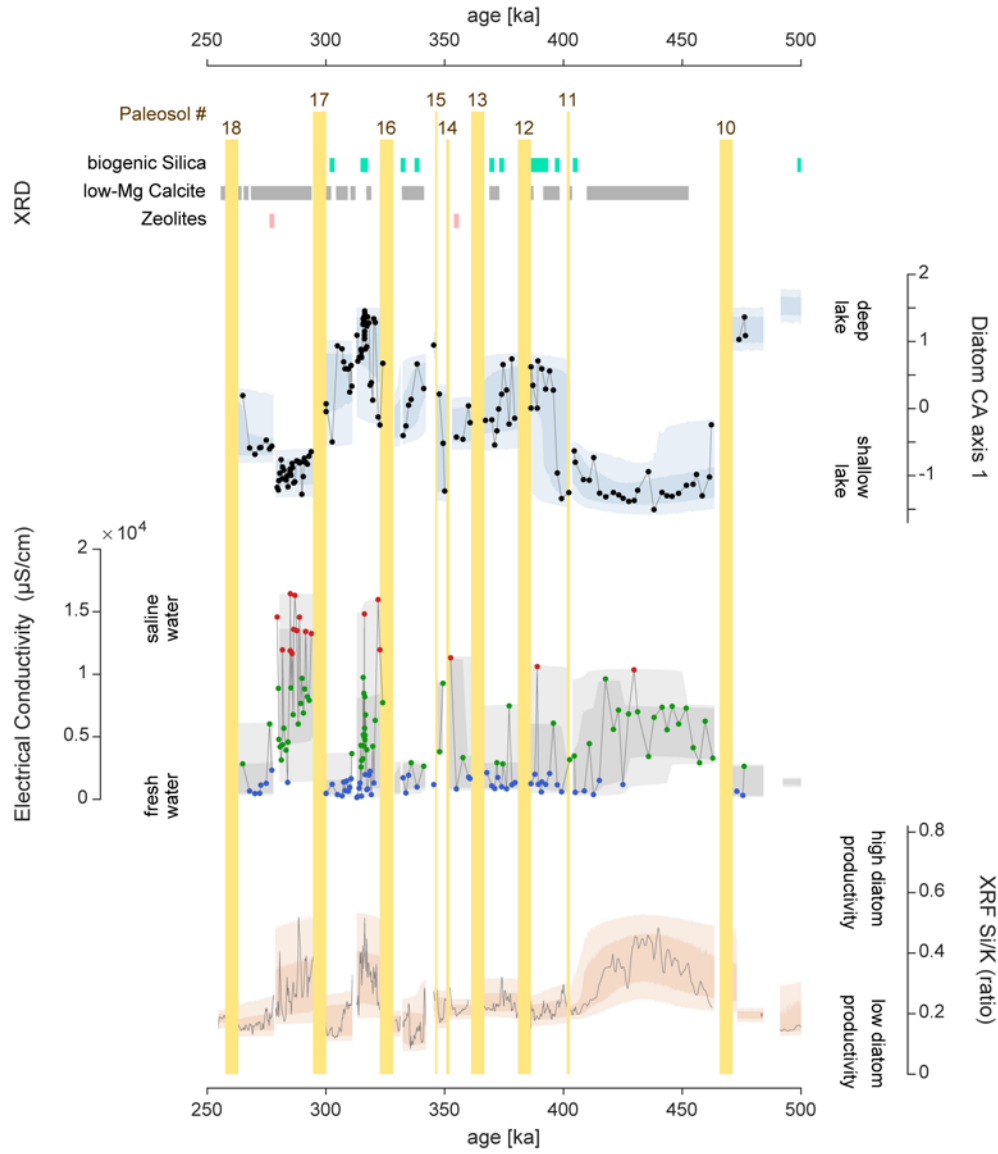
1426 relative to other local taxa (wetland Cyperaceae). Coverage in the time window between ~400 to

1427 300 ka is modest. By contrast, the Koora basin core exhibits evidence of strong fluctuation in

1428 woody-grassy vegetation, including times of predominantly woody vegetation (and

1429 predominantly tall grass; Iph index, Fig. 3B), with no overall vegetation trend toward drier
1430 conditions. $\delta^{13}\text{C}_{\text{wax}}$ and $\delta^{13}\text{C}_{\text{org}}$ also show strong shifts between grassy and wooded conditions
1431 (Fig. 3B), providing further support for different vegetation and water supply histories in the two
1432 basins over the past 600,000 years.

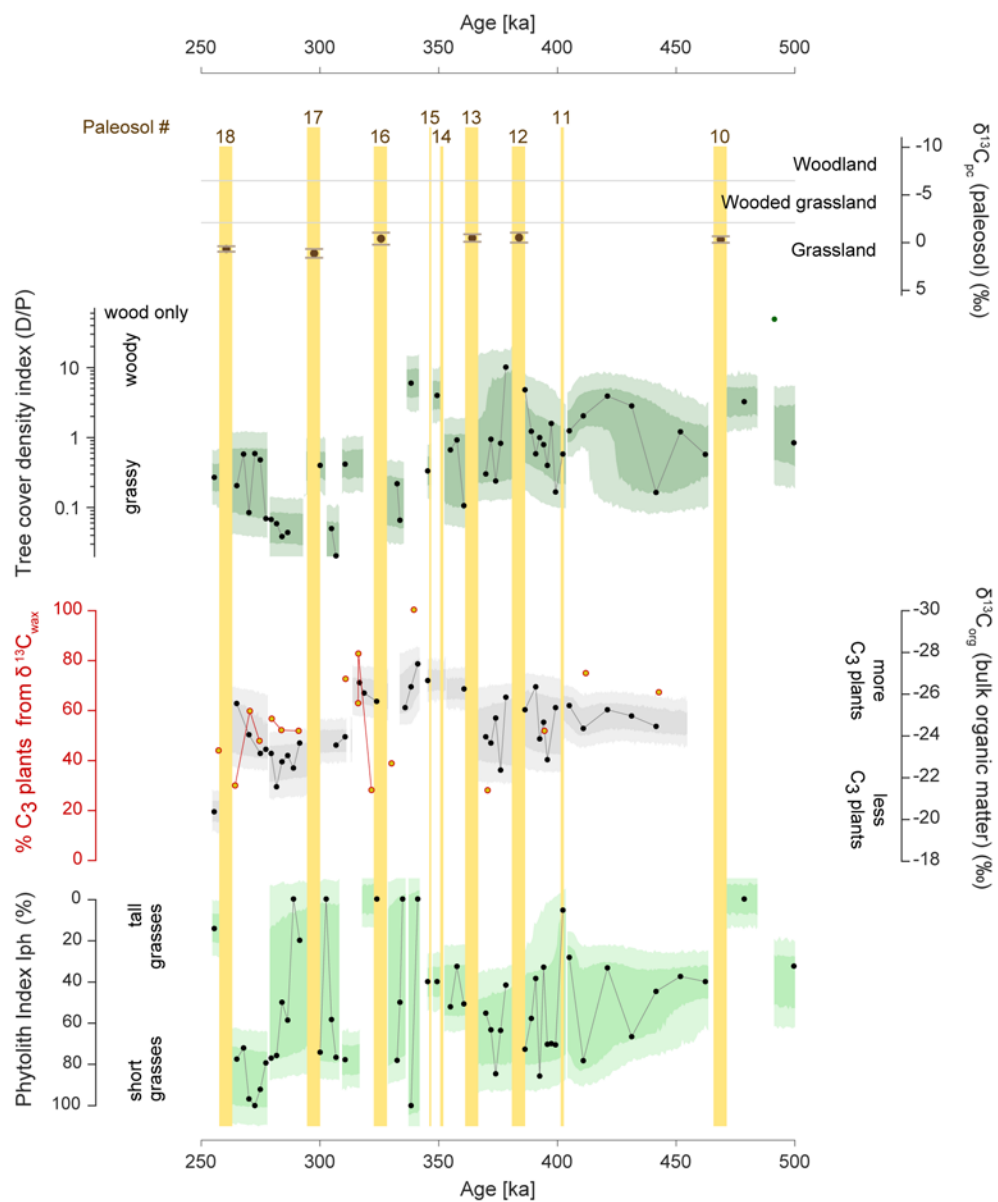
1433

A

1434

1435 **Fig. S9.**1436 **Expanded data sets covering the critical window between 500 ka and 300 ka. (A)** water1437 availability and **(B)** vegetation dynamics, enlarged from main text Fig. 3A and 3B.

1438

B

1440

1441

1442

1443 **Supplementary Data Tables**

1444 **Table S3.**

1445 **Supplementary Data: Diatom taxa percentages on the drilled meters below surface depth**
1446 **scale (R. B. Owen)**

1447 [Uploaded separately]

1448

1449 **Table S4.**

1450 **Supplementary Data: Diatom CA axis 1 (dimensionless scores), on age model time scale with**
1451 **median ages and uncertainties (a) (R. B. Owen)**

1452 [Uploaded separately]

1453

1454 **Table S5.**

1455 **Supplementary Data: Diatom electrical conductivity (EC), on age model time scale with**
1456 **median ages and uncertainties (a) (R. B. Owen)**

1457 [Uploaded separately]

1458

1459 **Table S6.**

1460 **Supplementary Data: Phytolith counts and indices on age model scale with median ages and**
1461 **uncertainties (a) (R. Kinyanjui)**

1462 [Uploaded separately]

1463

1464 **Table S7.**

1465 **Supplementary Data: Carbon and oxygen isotope values of pedogenic carbonates samples**
1466 **from Koora basin core ODP-OLO12-1A, showing isotope data for each sample used to**

1467 **calculate the mean paleosol $\delta^{13}\text{C}$ value, on meters below surface depth scale (see Table S8)**

1468 **(J.W. Moerman, N.E. Levin)**

1469 [Uploaded separately]

1470

1471 **Table S8.**

1472 **Supplementary Data: Mean pedogenic carbonate carbon and oxygen isotope data for**

1473 **paleosols in Fig. 3B in Koora basin core ODP-OLO12-1A, on age model scale. Mean values**

1474 **are shown for each paleosol in Fig. 3B. (J.W. Moerman, N.E. Levin)**

1475 [Uploaded separately]

1476

1477 **Table S9.**

1478 **Supplementary Data: XRF core scanning for Si/K ratio on age model time scale with**

1479 **median ages and uncertainties (a) (M. Stockhecke)**

1480 [Uploaded separately]

1481

1482 **Table S10.**

1483 **Supplementary Data: XRD data on age model time scale with median ages and uncertainties**

1484 **(a) (N. Rabideaux, D. Deocampo)**

1485 [Uploaded separately]

1486

1487 **Table S11.**

1488 **Supplementary Data: $\delta^{13}\text{C}$ -leafwax, percent C_3 leaf waxes on age model time scale with**

1489 **median ages and uncertainties (a) (J.M. Russell, R. Lupien)**

1490 [Uploaded separately]

1491

1492 **Table S12.**
1493 **Supplementary Data: $\delta^{13}\text{C}$ bulk organic matter on age model time scale with median ages**
1494 **and uncertainties (a) (J.M. Russell, R. Lupien)**
1495 [Uploaded separately]